Low-Frequency Divergence and Quantum Geometry of the Bulk Photovoltaic Effect in Topological Semimetals

Junyeong Ahn[1,2,*] Guang-Yu Guo,[3,4,†] and Naoto Nagaosa[1,2,‡]

[1]*RIKEN Center for Emergent Matter Science (CEMS), Wako, Saitama 351-0198, Japan*
[2]*Department of Applied Physics, The University of Tokyo, Bunkyo, Tokyo 113-8656, Japan*
[3]*Department of Physics and Center for Theoretical Physics, National Taiwan University,*
Taipei 10617, Taiwan
[4]*Physics Division, National Center for Theoretical Sciences, Hsinchu 30013, Taiwan*

We study the low-frequency properties of the bulk photovoltaic effect in topological semimetals. The bulk photovoltaic effect is a nonlinear optical effect that generates dc photocurrents under uniform irradiation, which is allowed by noncentrosymmetry. It is a promising mechanism for a terahertz photodetection based on topological semimetals. Here, we systematically investigate the low-frequency behavior of the second-order optical conductivity in point-node semimetals. Through symmetry and power-counting analysis, we show that Dirac and Weyl points with tilted cones show the leading low-frequency divergence. In particular, we find new divergent behaviors of the conductivity of Dirac and Weyl points under circularly polarized light, where the conductivity scales as ω^{-2} and ω^{-1} near the gap-closing point in two and three dimensions, respectively. We provide a further perspective on the low-frequency bulk photovoltaic effect by revealing the complete quantum geometric meaning of the second-order optical conductivity tensor. The bulk photovoltaic effect has two origins, which are the transition of electron position and the transition of electron velocity during the optical excitation, and the resulting photocurrents are, respectively, called the shift current and the injection current. Based on an analysis of two-band models, we show that the injection current is controlled by the quantum metric and Berry curvature, whereas the shift current is governed by the Christoffel symbols near the gap-closing points in semimetals. Finally, for further demonstrations of our theory beyond simple two-band models, we perform first-principles calculations on the shift and injection photocurrent conductivities as well as geometric quantities of antiferromagnetic $MnGeO_3$ and ferromagnetic PrGeAl, respectively, as representatives of real magnetic Dirac and Weyl semimetals. Our calculations reveal gigantic peaks in many nonvanishing elements of photoconductivity tensors below a photon energy of about 0.2 eV in both $MnGeO_3$ and PrGeAl. In particular, we show the ω^{-1} enhancement of the shift conductivity tensors due to the divergent behavior of the geometric quantities near the Dirac and Weyl points as well as slightly gapped topological nodes. Moreover, the low-frequency bulk photovoltaic effect is tunable by carrier doping and magnetization orientation rotation. Our work brings new insights into the structure of nonlinear optical responses as well as the design of semimetal-based terahertz photodetectors.

*Present address: Department of Physics, Harvard University, Cambridge, MA 02138, USA;
junyeongahn@fas.harvard.edu
†gyguo@phys.ntu.edu.tw
‡nagaosa@riken.jp

I. INTRODUCTION

Topological semimetals are emerging as efficient infrared and terahertz photodetectors [1]. In contrast to semiconductors whose absorption spectrum is bounded below by the band gap, semimetals can detect radiations down to the terahertz range because of their gapless spectrum. A promising mechanism for the generation of photocurrents in semimetals is the bulk photovoltaic effect. It refers to the generation of photocurrents under uniform irradiation of light due to the intrinsic inversion asymmetry of the system. Since the bulk photovoltaic effect does not require a bias voltage for breaking inversion symmetry, dark current noise can be suppressed [1].

To achieve high photosensitivity, we need to understand how to obtain large photoconductivity. It is believed that band topology plays an important role [2–6]. The bulk photovoltaic effect occurs due to the inversion-asymmetric transition of electron position or velocity during the optical excitation, and the resulting photocurrents are, respectively, called the shift current and the injection current [7]. In nonmagnetic systems, linearly polarized light induces shift currents, while circularly polarized light induces injection currents. Remarkably, both the linear shift [4] and circular injection [5] currents were found to be intimately related to the topological quantities, the Berry connection and the Berry curvature, respectively. These discoveries have led to various theoretical and experimental studies searching for topological enhancement near the gap-closing points [8–19].

However, while there is a concrete proportional quantitative relationship between the injection current and the Berry curvature, no such quantitative relation exists between the shift current and the Berry connection. For example, a Dirac point (DP) in two dimensions has a quantized π Berry phase and thus has a nontrivial Berry connection. Nevertheless, such a Dirac point does not generate a shift current because of its inversion symmetry. Furthermore, no simple quantitative relation was found between the shift current and the shift vector [20], a gauge-invariant quantity related to the Berry connection, without some special requirements like the momentum independence of the dipole matrix elements [21].

The bulk photovoltaic effect in magnetic topological semimetals is more poorly understood, although a recent work has revealed some general aspects [22]. Because of time-reversal symmetry breaking in magnetic systems, linearly (circularly) polarized light can generate injection (shift) currents as well as shift (injection) currents. There are some works highlighting the generation of large linear injection currents in magnetic systems [22–27], but the relationship between the response and band topology has not been understood. Moreover, there has been very little focus on the circular shift current, while the first concept of

the shift current appeared as a response to circularly polarized light [28–30]. One reason for this lack of attention is that injection currents are typically stronger than the shift currents. Since there is rapid progress in the experimental observation [31–33] and theoretical proposal [34–42] of various magnetic topological semimetals, addressing optical properties in magnetic topological semimetals is now a timely subject.

In this work, we reveal general low-frequency properties of the shift and injection currents in magnetic and non-magnetic point-node semimetals. By employing symmetry and power-counting analysis, we determine the leading low-frequency divergence near the gap-closing point, as summarized in Table I. We show that tilted DP and Weyl points (WPs) can generate the leading divergence. While the bulk photovoltaic response in tilted Dirac and Weyl points have been studied [13,23–25], here we approach them in a unified way and discover new aspects. Our theory covers type-I and type-II spectrums of Dirac and Weyl points in any dimensions. In particular, our analysis includes type-II Dirac points in two dimensions and type-I and type-II Dirac points in three dimensions, which are relevant to magnetic Dirac semimetals, whose shift and injection currents have not been previously studied. It is widely known that the protection of Dirac points against opening the gap requires inversion symmetry, which forbids the bulk photovoltaic response. It is true in non-magnetic systems. However, in magnetic systems, symmetry under the combination of spatial inversion P and time reversal T, which is PT symmetry, is enough for the protection [39–42], so inversion symmetry can be broken. Also, we study the largely overlooked circular shift current in Weyl and Dirac systems. The circular shift current grows fast as the photon frequency gets smaller, and it scales as ω^{-1} in three dimensions. These results indicate that Dirac semimetals in three dimensions can show divergent photovoltaic responses like Weyl semimetals, although the Berry curvature is identically zero due to PT symmetry. In two dimensions, it grows faster as ω^{-2}.

TABLE I. Low-frequency properties of second-order dc photovoltaic responses. Linear and circular indicate the polarization of light. Injection and shift conductivities are defined by Eq. (4). The sign $\pm$ indicates the parity of the conductivity tensor under the action of time reversal T and spacetime-inversion PT. See Eqs. (9) and (10). In T- (PT-) symmetric systems, only the responses with the positive T- (PT-) parity appear. All four responses can appear when T and PT symmetries are both broken. Based on their symmetry properties, we call the linear injection and circular shift current responses PT-symmetric responses and the linear shift and circular injection current responses T-symmetric responses. Symplectic Christoffel symbols indicate the symplectic analog of the Christoffel symbol of the first kind [see Eq. (33)]. Here, we consider only interband-transitive processes in the clean limit, where the relaxation rate $\Gamma = \tau^{-1}$ is smaller than the photon frequency ω. In this case, the injection current is typically larger than the shift current, and they become comparable when ω approaches Γ.

Response	Linear injection	Circular injection	Linear shift	Circular shift
Parity under T	$-$	$+$	$+$	$-$
Parity under PT	$+$	$-$	$-$	$+$
Geometric quantities	Quantum metric	Berry curvature	Symplectic Christoffel symbols	Christoffel symbols of the first kind
Leading divergence	$O(\tau\omega^{d-3})$		$O(\omega^{d-4})$	

We find that tilted Dirac and Weyl points show what we call the separation of responses, where photocurrents of different origins manifest through different current directions. For example, circular shift and circular injection currents flow in different directions. This property can be useful in the detection of shift currents in the coexistence of the stronger injection currents. The separation of responses can occur from the symmetry transformation property under magnetic operations MT or C_2T, where M and C_2 are mirror and twofold rotation, so it remains robust in the system beyond the **k**-linear approximation as long as those symmetries are preserved.

Our symmetry and power-counting analyses are sufficient for understanding the general pattern of the response for systems with a linear spectrum. However, for a deeper understanding of the response, we propose a new perspective on the low-frequency bulk photovoltaic effect. We uncover the full geometric nature of shift and injection currents. Here, as well as in the Berry curvature, another geometric quantity called the quantum metric has a crucial role. Since geometry has more information than topology about quantum states, we observe the consequence of band topology in a more broad perspective through geometric quantities. We show that the linear injection conductivity is determined only by the quantum metric near the gap closing, in the same way as the circular injection conductivity is determined by the Berry curvature, which completes the geometric understanding of the injection currents at the low-frequency regime. Furthermore, we show that the shift conductivities are related to more interesting quantities, which are the Christoffel symbols. Unlike the Berry connection, which has a complicated relationship to the magnitude of the shift current, the Christoffel symbols directly control the magnitude of the response. In this viewpoint, the enhancement of the shift and injection current responses near the gap-closing point can be attributed to the divergence of the geometric quantities at the geometric singularity, i.e., the gap-closing point. Furthermore, our unique perspective allows us to view the bulk photovoltaic effect as novel tools for experimental measurements of quantum geometry in materials.

Our geometric interpretation of the bulk photovoltaic effect is clearly distinguished from the one in Ref. [22], which also discusses the role of the quantum metric. In Ref. [22], the shift current is decomposed into four parts, and one of them is interpreted as the geometric contribution. The injection current is identified as having no geometric origin. These are in contrast to our interpretation in which both shift and injection currents are fully geometric responses. Only through our direct quantitative relationships can the bulk photovoltaic effect be identified as a useful measure of quantum geometry in experiments as well as a way to theoretically understand the low-frequency divergent behavior.

Finally, for further demonstrations of our theory beyond simple two-band models, we perform first-principles relativistic band theoretical calculations of the shift and injection photocurrent conductivities as well as geometric quantities in antiferromagnetic (AF) $MnGeO_3$ and ferromagnetic (FM) PrGeAl (as will be reported in Sec. VI below), respectively, as representatives of real magnetic Dirac and Weyl semimetals. In AF $MnGeO_3$, although both T and P symmetries are broken, the combined PT symmetry is preserved [42]. Thus, AF $MnGeO_3$ was recently predicted to be a rare magnetic Dirac semimetal [42]. As our theory predicts (Table I), we find nonzero elements of circular shift and linear injection photoconductivity tensors in AF $MnGeO_3$. In fact, several nonzero elements exhibit huge peaks below a photon energy of about 0.2 eV. Our calculations reveal that there are at least there Dirac points in the vicinity of the Fermi level, and two of the Dirac points are each accompanied by a slightly gapped Dirac point. The calculated quantum metric and Christoffel symbol of the first kind exhibit divergent behaviors near both the gapless and gapped Dirac points, thus leading to the geometric enhancement in linear injection and circular shift currents, respectively. In contrast, both T and PT symmetries are broken in FM PrGeAl [43], and hence all four types of the bulk photovoltaic effect may emerge in FM PrGeAl, as our theory predicts (Table I). Indeed, we find that many nonzero elements of all shift and injection conductivity tensors show gigantic peaks in the low-frequency range up to 0.1 eV. There are at least 160 type-I and type-II Weyl points within ± 0.1 eV of the Fermi level in FM PrGeAl [43]. Our calculations indicate that the low-frequency peaks can be further increased by up to a factor of 5 by raising the chemical potential from the Fermi level to the energy of certain Weyl points. Our calculations also reveal the divergent behaviors of both the quantum geometric tensor and the quantum geometric connection (symplectic Christoffel symbol and Christoffel symbol of the first kind) near the Weyl points and also anticrossing topological nodes, thus leading to the gigantic low-frequency shift and injection currents in FM PrGeAl. Furthermore, we notice that FM PrGeAl is a soft ferromagnet [44]. Thus, the magnetization direction can be easily rotated away from the easy c axis to, e.g., the a axis, which may cause a topology change of the Weyl-point distribution in the Brillouin zone (BZ) [43], thereby resulting in significant changes in the shift and injection photoconductivities. Also, since the circular shift and injection conductivity tensors are antisymmetric with respect to the magnetization direction, they would change sign when the magnetization direction is reversed. All these observations show that the gigantic low-frequency shift and injection photocurrents in FM PrGeAl can be tuned by either carrier doping or magnetization direction rotation.

The outline of this paper is as follows. We explain the shift and injection currents as a second-order optical response in Sec. II. Then, we study the symmetry and low-frequency divergence of the shift and injection currents

in Sec. III. Section IV enriches our analysis by revealing the quantum geometrical nature of the low-frequency responses. We elaborate more on the symmetry and divergence with concrete models and numerical calculations in Sec. V. In Sec. VI, we present our first-principles calculations on the shift and injection photocurrent conductivities as well as geometric quantities of AF MnGeO$_3$ and FM PrGeAl. In particular, we analyze the gigantic peaks in the calculated low-frequency photoconductivity spectra in MnGeO$_3$ and PrGeAl in terms of the divergent behaviors of the geometric quantities near the gapless and slightly gapped topological nodal points. Finally, we discuss several issues about the low-frequency divergence in Sec. VII.

II. SHIFT AND INJECTION CURRENTS

Let us expand current density j in increasing powers of the electric field E as

$$j^c = \sigma^{c;a}_{(1)}E_a + \sigma^{c;ab}_{(2)}E_aE_b + \sigma^{c;abc}_{(3)}E_aE_bE_c + \cdots. \quad (1)$$

The first term is the familiar linear response, and the other terms are nonlinear responses. Since the current density oscillates in-phase with the electric field in the linear response, the dc photocurrent generation is inherently a nonlinear optical effect. In our work, we assume that the electric field is sufficiently small such that perturbation theory works (we discuss in Sec. VII how small it should be). While even-order responses to E vanish in centrosymmetric systems, they are allowed in noncentrosymmetric systems. The bulk photovoltaic effect studied in the present paper is thus primarily a second-order response.

The second-order optical response under the uniform illumination of light has the form $j^c(\omega_1 + \omega_2) = \sigma^{c;ab}(\omega_1 + \omega_2; \omega_1, \omega_2)E_a(\omega_1)E_b(\omega_2)$, in general. Let us focus on the dc generation

$$j^c_{dc} = \sigma^{c;ab}_{dc}(\omega)E_a(\omega)E_b(-\omega), \quad (2)$$

where $j^c_{dc} = j^c(0)$ and $\sigma^{c;ab}_{dc}(\omega) = \sigma^{c;ab}(0; \omega, -\omega)$. In the clean limit—where the interband relaxation rate is smaller than the photon frequency and the band gap, interband transitions are described by two processes: shift and injection [45]:

$$\sigma^{c;ab}_{dc} = \sigma^{c;ab}_{shift} + \sigma^{c;ab}_{inj}. \quad (3)$$

The shift and injection currents correspond to the current generated by the change of the electron position and velocity, respectively, during the interband transition of electrons [7]. One can see this correspondence by noting that the shift and injection conductivities have the form of the Fermi golden rule [7] (see the Appendix B for explicit calculations). Explicitly, they have the form [47,48]

$$\sigma^{c;ab}_{shift} = -\frac{\pi e^3}{\hbar^2}\int_{\mathbf{k}}\sum_{n,m}f^{FD}_{nm}(R^{c,a}_{mn} - R^{c,b}_{nm})r^b_{nm}r^a_{mn}\delta(\omega_{mn} - \omega),$$

$$\sigma^{c;ab}_{inj} = -\tau\frac{2\pi e^3}{\hbar^2}\int_{\mathbf{k}}\sum_{n,m}f^{FD}_{nm}\Delta^c_{mn}r^b_{nm}r^a_{mn}\delta(\omega_{mn} - \omega), \quad (4)$$

where $\int_{\mathbf{k}} = \int d^dk/(2\pi)^d$, f^{FD}_n is the Fermi-Dirac distribution of the band n, $f^{FD}_{nm} = f^{FD}_n - f^{FD}_m$, $\hbar\omega_{mn} = \hbar\omega_m - \hbar\omega_n$ is the energy difference between bands m and n, $H|n\rangle = \hbar\omega_n|n\rangle$, $r^a_{mn} = \langle m|i\partial_a|n\rangle$, $v^c_{mn} = \hbar^{-1}\langle m|\partial_c H|n\rangle$, and we use the notation $\partial_a = \partial/\partial k_a$. Note that $R^{c,a}_{mn} = r^c_{mm} - r^c_{nn} + i\partial_c \log r^a_{mn}$ is called the shift vector—characterizing the interband transition of the displacement—and $\Delta^c_{mn} = v^c_{mm} - v^c_{nn}$ is the interband transition of the velocity. Here, τ is the relaxation time that saturates the injection current: Without it, the injection of moving electrons and holes leads to a constant growth in time. We take the electron charge as $-e$ (i.e., $e > 0$). Equation (4) is valid with and without time-reversal symmetry.

III. SYMMETRY AND POWER-COUNTING ANALYSIS

To get a general perspective on the low-energy properties of the shift and injection currents, we review their symmetry properties and then study the pattern of low-frequency divergences. The key properties presented in this section are summarized in Table I, and they serve as basic ingredients for the analysis in Sec. V.

A. Symmetry of the shift and injection conductivities

Let us first decompose the second-order dc conductivity into its real and imaginary parts:

$$\sigma^{c;ab}(\omega) = \sigma^{c;ab}_L(\omega) + i\sigma^{c;ab}_C(\omega). \quad (5)$$

Using $E^*(\omega) = E(-\omega)$ and Eq. (2), one can see that the conductivity can be symmetrized such that

$$\sigma^{c;ab}_L(\omega) = \sigma^{c;ba}_L(\omega),$$
$$\sigma^{c;ab}_C(\omega) = -\sigma^{c;ba}_C(\omega). \quad (6)$$

Therefore, we always consider conductivity tensors satisfying Eq. (6). We note that the expressions in Eq. (4) are already symmetrized. Assuming the form $\mathbf{E}(t) = |E|e^{-i\omega t}(\cos\phi, \sin\phi, 0) + $ c.c. for linearly polarized light and $\mathbf{E}(t) = |E|e^{-i\omega t}(1, i, 0) + $ c.c. for circularly polarized light, the generated photocurrent is

$$j^c_{L-dc} = (\sigma^{c;xx}_L\cos^2\phi + \sigma^{c;yy}_L\sin^2\phi$$
$$+ 2\sigma^{c;xy}_L\sin\phi\cos\phi)|E^2|$$
$$j^c_{C-dc} = (\sigma^{c;xx}_L + \sigma^{c;yy}_L - 2\sigma^{c;xy}_C)|E^2|. \quad (7)$$

The real part of the conductivity is responsible for the current generation regardless of the polarization, while the imaginary part of the conductivity is responsible for the current

generated by the circularly polarized light. If one measures the current difference between the ones generated by left-circularly polarized light and right-circularly polarized light $\propto \sigma^{c;xy} - \sigma^{c;yx}$, only the imaginary part contributes. In the following, we call the real part $\sigma_L^{c;ab}$ linear conductivity and the imaginary part $\sigma_C^{c;ab}$ circular conductivity.

From the definition in Eq. (2) and the transformation properties of the current and electric field, it is clear that the second-order optical conductivity transforms like a third-rank tensor under spatial transformations. In other words, $\sigma'^{c_1;a_1 b_1}_{\mathrm{dc}} = \mathcal{M}_{c_1 c} \mathcal{M}_{a_1 a} \mathcal{M}_{b_1 b} \sigma^{c;ab}_{\mathrm{dc}}$ under a point-group symmetry transformation $x_a \to x'_a = \mathcal{M}_{ab} x_b$. [49] However, one should be careful when taking time reversal for relaxational processes as is well known from the Onsager reciprocity relations in linear response theory [50–52]. For example, it seems like Eq. (2) implies that time reversal reverses the sign of the dc conductivity for linearly polarized light. However, we need to additionally reverse the sign of the phenomenological relaxation rate Γ in order to make the decay in time to the growth in time. The correct time reversal for the second-order dc conductivity is

$$\sigma_{\mathrm{dc}}^{c;ab}(\omega, \Gamma) \to \sigma'^{c;ab}_{\mathrm{dc}}(\omega, \Gamma) = -\sigma_{\mathrm{dc}}^{c;ba}(\omega, -\Gamma). \quad (8)$$

See Appendix C. When applying this equality, the delta function and τ should be interpreted as $\pi^{-1}\Gamma/[(\omega_{mn} - \omega)^2 + \Gamma^2]$ and Γ^{-1}, so they reverse sign under $\Gamma \to -\Gamma$. Thus, the real part of the shift and injection conductivity tensor transforms as

$$\sigma'^{c_1;a_1 b_1}_{\mathrm{shift,L}} = \mathcal{M}_{c_1 c} \mathcal{M}_{a_1 a} \mathcal{M}_{b_1 b} \sigma^{c;ab}_{\mathrm{shift,L}},$$
$$\sigma'^{c_1;a_1 b_1}_{\mathrm{inj,L}} = (-1)^{s_T} \mathcal{M}_{c_1 c} \mathcal{M}_{a_1 a} \mathcal{M}_{b_1 b} \sigma^{c;ab}_{\mathrm{inj,L}}, \quad (9)$$

and the imaginary part transforms as

$$\sigma'^{c_1;a_1 b_1}_{\mathrm{shift,C}} = (-1)^{s_T} \mathcal{M}_{c_1 c} \mathcal{M}_{a_1 a} \mathcal{M}_{b_1 b} \sigma^{c;ab}_{\mathrm{shift,C}},$$
$$\sigma'^{c_1;a_1 b_1}_{\mathrm{inj,C}} = \mathcal{M}_{c_1 c} \mathcal{M}_{a_1 a} \mathcal{M}_{b_1 b} \sigma^{c;ab}_{\mathrm{inj,C}}, \quad (10)$$

under the spacetime symmetry transformation $(t, x_a) \to (t', x'_a) = ((-1)^{s_T} t, \mathcal{M}_{ab} x_b)$. Alternatively, one can verify these transformation rules by examining transformations of $R^{c,a}_{mn}$, r^a_{nm}, and Δ^c_{mn} from the form in Eq. (4). See Appendix D for a derivation.

Knowing these symmetry transformation properties, one can use MTENSOR [53] in the Bilbao Crystallographic Server to see which tensor components are required to vanish by symmetry for any of 80 magnetic point groups. For our purposes, the most important symmetries are simply time-reversal T and spacetime-inversion PT symmetries (note, again, that P is always broken in the present paper). We summarize their role in Table I. While only linear shift and circular injection currents can be generated

in time-reversal-symmetric systems, they vanish in PT-symmetric systems; thus, linear injection and circular shift currents can be generated, and therefore, time-reversal symmetry and spacetime-inversion symmetry are complementary to each other, as pointed out in Ref. [22]. This behavior is manifested in the geometric quantities related to the responses. As we show below in Sec. IV, T-symmetric responses are related to both the Berry curvature and the quantum metric, while PT-symmetric responses are related to the quantum metric only. In general magnetic systems without T and PT symmetries, all four types of currents can be generated.

When there is MT or $C_2 T$ symmetry instead, where M and C_2 are mirror and twofold rotation, a phenomenon of "separation of responses" occurs, meaning that different directions manifest different types of responses, because those symmetries act like time-reversal symmetries in some directions and act like spacetime-inversion symmetries in the other directions. For example, $M_x T$ acts like time-reversal symmetries in the y and z directions, whereas it acts as spacetime-inversion symmetry in the x direction. In this case, x-polarized light generates a shift current along y and z while generating an injection current along x. We demonstrate the separation of responses through model calculations in Sec. V and also through first-principles calculations in Sec. VI.

B. Power-counting analysis of the low-energy divergence

Let us now examine the low-energy divergence of the second-order responses in semimetals. We can estimate the divergence by counting the power of photon frequency in Eq. (4). Since the delta function has dimension ω^{-1}, R^c and r^a_{mn} have dimension k^{-1}, and Δ^c has dimension ω/k, the shift and injection conductivity scales as

$$\sigma_{\mathrm{shift}}^{c;ab} \sim \frac{e^3}{\hbar^2} \frac{1}{\omega} k^{d-3},$$
$$\sigma_{\mathrm{inj}}^{c;ab} \sim \frac{e^3}{\hbar^2} \tau k^{d-3}, \quad (11)$$

where k is the characteristic wave vector. When the system has dispersion $E \propto k^\alpha$, $k \sim E^{1/\alpha} \sim \omega^{1/\alpha}$. Thus, a smaller α is preferred to get large optical responses for small ω in 2D, while it is independent of the dispersion in 3D.

In lattice systems, stable Weyl points (and also Dirac points protected by symmorphic symmetries [54]) always appear pairwise according to the Nielsen-Ninomiya theorem [55,56]. Therefore, a response in semimetals should be a sum of responses from different Weyl or Dirac points. However, different gap-closing points are located at different energy levels, in general, so it is expected that only a particular point contributes to the low-energy response significantly [5]. An exact cancellation or reinforcement among different gap-closing points can occur due to

symmetries, but it can be considered straightforwardly from the symmetry transformation properties of the conductivity tensor. In this regard, the response from a single gap-closing point can be associated with the low-energy response of a whole system.

Thus, we consider a gap-closing point with a linear dispersion, described by a Dirac Hamiltonian

$$H_0(\mathbf{k}) = \hbar v \sum_{a=1}^{d} k_a \Gamma_a, \tag{12}$$

where Γ_a are mutually anticommuting matrices, such that the spectrum has the form

$$E(\mathbf{k}) = \pm \hbar v |\mathbf{k}|. \tag{13}$$

In this case, we have

$$\sigma_{\text{shift}}^{c;ab} \sim \frac{e^3}{\hbar^2} \frac{1}{\omega} \left(\frac{v}{\omega}\right)^{3-d},$$

$$\sigma_{\text{inj}}^{c;ab} \sim \frac{e^3}{\hbar^2} \tau \left(\frac{v}{\omega}\right)^{3-d} \tag{14}$$

through a dimensional analysis. This divergence is expected to occur in the absence of a symmetry cancellation. However, Eq. (12) has too many symmetries, so we need to break them, in general. A Dirac point has inversion symmetry (by definition, it is nonchiral), so the second-order optical response is forbidden. Also, as noted in Refs. [13,22,25], a Weyl point described by Eq. (12) does not show a second-order optical response by linearly polarized light because Eq. (12) has SO(d) rotational symmetry in d spatial dimensions. In 3D, the absence of mirror symmetry (chirality) in Weyl semimetals allows one unique nonvanishing independent component $\sigma_{\text{inj},C}^{3;12}$ under circularly polarized light. Because a Weyl point in 3D has time-reversal symmetry around the gap-closing point, the circular shift current is also forbidden, and the generated dc current is the circular injection current. Even for a more general linear dispersion described by $H = \sum_{a,i=1}^{d} \hbar v_{ai} k_a \Gamma_i$, which apparently has less symmetry, only circular injection currents for a Weyl point can be nonvanishing because the conductivity for this Hamiltonian is given by $\sigma_{\text{dc}}^{c;ab} = v^{-3} v_{ai} v_{bj} v_{ck} \det(v_{ai}/v) \sigma_{\text{dc},0}^{k;ij}$ [13], where $\sigma_{\text{dc},0}^{k;ij}$ is the conductivity for $v_{ai} = v \delta_{ai}$, which is the case for Eq. (12) (see Appendix F for a derivation).

The only way to generate the leading divergence for shift currents and linear injection currents is to tilt the Dirac or Weyl cone, as shown in Fig. 1. Since it allows anisotropic optical excitations around the gap-closing point, photocurrents can flow whose direction depends on the direction of the tilting. To see that other symmetry breaking gives subleading power in ω^{-1}, let us add symmetry-breaking perturbations to the Dirac Hamiltonian,
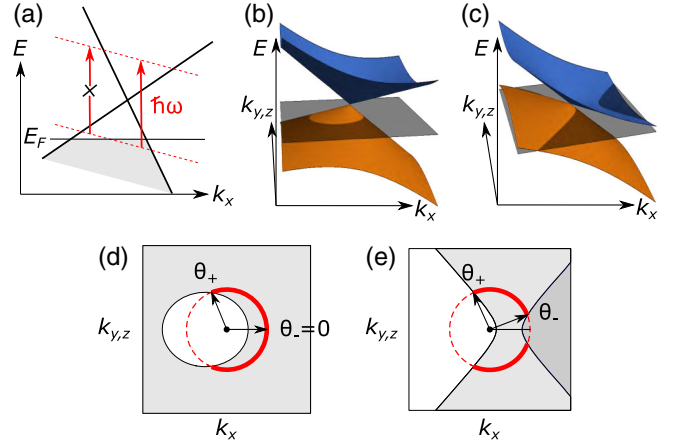

FIG. 1. Optical excitation near a tilted Dirac or Weyl cone. (a) Excitation of electrons by the absorption of a photon with frequency ω. (b) Type-I spectrum, $|v'/v| < 1$. (c) Type-II spectrum, $|v'/v| > 1$. Here, v is the velocity of a Dirac or Weyl fermion at zero tilting, and v' is the overall velocity shift by $\mu \to \mu + \hbar v' k_x$, giving rise to a tilting of the cone. The gray planes in panels (b) and (c) show the Fermi level. (d,e) Optically active region in momentum space for (d) type-I and (e) type-II cases. The small black dots at the center indicate the location of the gap-closing point. Red circles around the points show the surface satisfying $\hbar\omega = \hbar\omega_c - \hbar\omega_v = 2\hbar vk$, where $k = 0$ at the gap closing. Both conduction and valence bands are unoccupied in the white region, only the valence band is occupied in the light gray region, and both bands are occupied in the gray region. Electrons can be optically excited only on the solid red arcs (i.e., $\theta_- < \theta < \theta_+$, where θ is the absolute value of the polar angle in either 2D or 3D), which is in the light gray region.

$$H(\mathbf{k}) = H_0(\mathbf{k}) + \hbar \sum_a \sum_{p=0}^{\infty} \lambda_{p,a} k^p \Gamma_a. \tag{15}$$

Here, $\lambda_{p,a}$ is a constant parameter, $\Gamma_{a\neq 0}$ are mutually anticommuting matrices, and we also include Γ_0 as the identity matrix. Since the dimensionless parameter is $\lambda_{p,a} k^p \omega^{-1} \sim \lambda_{p,a} \omega^{p-1}$, responses due to perturbations in $\lambda_{p,a}$ have weaker low-frequency divergences for $p > 1$. For example, let us consider a quadratic correction, resulting in the dispersion relation $E = \pm(\hbar vk + \lambda_2 k^2)$. Optical excitations occur in the region satisfying $\omega = E_+ - E_- = 2(\hbar vk + \lambda_2 k^2)$, i.e., $k = \omega/v(1 - \lambda_2 \omega/v^2) + O(\omega^3)$. By inserting this into Eq. (11), we have corrections to the leading divergence by a fraction $|(d-3)\lambda_2 \omega/v^2| \ll 1$ for small ω. At the $p = 0$ order, $\lambda_{0,a}$ comes as either the chemical potential, the shift of the location of the gap-closing point, or a mass term [57]; i.e., we can write the Hamiltonian as $H(\mathbf{k}) = -\mu + \sum_{a=1}^{d}(k - k_0)_a \Gamma_a + M \sum \Gamma_{a>d}$. None of them generates a nonvanishing shift or linear injection currents. Note that μ breaks no symmetry, $\mathbf{k} - \mathbf{k}_0$ can be redefined as $\mathbf{k}$ such that the gap closes at $\mathbf{k} = 0$, and the mass term can serve as an inversion symmetry operator so that it forbids second-order optical responses. Let us now consider

$p = 1$. As we show above, the linear spectrum without tilting has zero shift and linear injection current responses. Thus, the remaining possibility is tilting the cone by adding $\lambda_{1,0} = -v' \cos\theta$, which gives an overall tilting of energy levels by $\mu \to \mu + v' k_x$.

Our analysis shows that the shift and injection conductivity tensors of tilted, massless Dirac and Weyl points have the form

$$\sigma_{\text{shift}}^{c;ab} = \frac{e^3}{\hbar^2} \frac{1}{\omega} \left(\frac{v}{\omega}\right)^{3-d} \mathcal{F}_{\text{shift}}^{c;ab}\left(\frac{2\mu}{\hbar\omega}, \frac{v'}{v}\right),$$

$$\sigma_{\text{inj}}^{c;ab} = \frac{e^3}{\hbar^2} \tau \left(\frac{v}{\omega}\right)^{3-d} \mathcal{F}_{\text{inj}}^{c;ab}\left(\frac{2\mu}{\hbar\omega}, \frac{v'}{v}\right). \quad (16)$$

Let us explain how the $\mathcal{F}$'s depend on v'/v and $2\mu/\hbar\omega$, in general. When $\mu \neq 0$, i.e., when the Fermi level is away from the gap-closing point, the chemical potential sets the lower bound for frequency, so the $\mathcal{F}$'s do not diverge as $\omega \to 0$.

When the Fermi level is exactly at the gap-closing point, i.e., $\mu = 0$, the $\mathcal{F}$'s show significantly different behavior for $|v'/v| < 1$ and $|v'/v| > 1$, which are called type I and type II [58], respectively [see Figs. 1(b) and 1(c)]. In the type-I case, tilting cannot generate shift and injection currents when $\mu = 0$ because, in this case, the Fermi surface is a point; thus, anisotropic excitation cannot occur. Therefore, only circular injection currents can be generated, which do not need tilting for their generation.

In contrast, in the type-II case, the Fermi surface has a finite size at $\mu = 0$, so anisotropic excitation can occur, in principle. However, it depends on whether the response is T symmetric or PT symmetric. While the T-symmetric responses (linear shift and circular injection) have a non-trivial response at $\mu = 0$ [13], the PT-symmetric responses (linear injection and circular shift) have a vanishing response at $\mu = 0$. This property is related to the fact that a Hamiltonian with only $\mathbf{k}$-linear terms has an emergent CPT symmetry, where C is the particle-hole operator, and $CPT = 1$: $(CPT)H(\mathbf{k})(CPT)^{-1} = -H(\mathbf{k})$. At $\mu = 0$, PT-symmetric responses should be zero since they also respect an effective C symmetry also [where $(PT)^{-1}$ takes the role of an effective C operator]—which reverses the direction of the current, while T-symmetric responses lack C symmetry and can be nontrivial.

Since PT-symmetric responses do not occur at $\mu = 0$, magnetic and nonmagnetic systems have the same low-frequency divergent behavior when $\mu = 0$ exactly. Nevertheless, as long as μ is small but not exactly zero, we can still expect enhanced PT-symmetric responses at small frequency $\omega \sim 2\mu/\hbar$ by the factor in front of the $\mathcal{F}$'s in Eq. (16). Therefore, PT-symmetric responses in magnetic systems can also show a divergent behavior associated with the $\omega \to 0$ limit with a fixed ratio of $2\mu/\hbar\omega$.

We investigate the symmetry properties of the tilted Dirac and Weyl points more closely in Sec. V by explicitly calculating the conductivity tensors. Before that, we derive the general formula for the shift and injection conductivities for arbitrary Dirac Hamiltonians and provide their geometric aspects in the following sections. This process adds more perspective on the transformation rule in Eqs. (9) and (10) and the divergent behavior near the gap-closing point.

IV. QUANTUM GEOMETRIC ASPECTS

In the previous section, we analyzed the overall trend of shift and injection currents using symmetry and power-counting analyses. Here, we show that every detail of the conductivity profile for the shift and injection currents is determined by quantum geometric quantities in the low-frequency regime. It was pointed out in Refs. [4,6] that the shift current is related to quantum geometry because the shift vector includes the Berry connection—a geometric quantity. Following these works, the geometric nature of the shift and injection currents was previously discussed in several works [5,22]. However, no simple quantitative relationship between the response and the geometric quantities has been found except for the circular injection conductivity [5]. In this section, we show that the shift and injection conductivities are proportional to geometric quantities that have natural geometric meaning on the Bloch sphere. These relationships are not limited to massless Dirac and Weyl points and are exact for any two-band system or PT-symmetric four-band system. It implies that interband-transitive photovoltaic responses at the low-frequency regime probe the quantum geometry of materials. In this perspective, the low-frequency divergence of the shift and injection current responses of gap-closing points can be attributed to their geometrically singular nature. Also, time-reversal symmetry transformations of the conductivity tensors, which are quite confusing, can be simply understood from the transformation properties of the geometric quantities. In the following, we first derive the formula that relates injection and shift currents with the Bloch vector of general Dirac Hamiltonians with an arbitrary matrix size in any spatial dimensions. Then, we provide a quantum geometric interpretation of our formula.

A. Shift and injection conductivity for Dirac Hamiltonians

We consider the low-energy effective model systems described by the following $d_M \times d_M$ Dirac Hamiltonian:

$$H(\mathbf{k}) = -\mu(\mathbf{k}) + \sum_i f_i(\mathbf{k})\Gamma_i, \quad (17)$$

where Γ_i are mutually anticommuting matrices. This Hamiltonian described a single Dirac or Weyl point when $f_i(\mathbf{k}) = k_i$; however, here, we do not need to assume linear

dispersion, and we consider a general form of $f_i(\mathbf{k})$'s. In particular, the above Hamiltonian describes general two-band Hamiltonians when $d_M = 2$, where $\Gamma_{i=1,2,3}$ are three Pauli matrices, and it describes general four-band PT-symmetric Hamiltonians [with $(PT)^2 = -1$] when $d_M = 4$, where $\Gamma_{i=1,\dots,5}$ are five Gamma matrices.

Let us express the injection and shift conductivities in terms of the f_i's. This method makes theoretical analysis and numerical calculations convenient. As for the injection current, one can integrate the delta function easily by using $\Delta_{mn}^c = \partial_c \omega_{mn}$ such that $\Delta_{mn}^c \delta(\omega_{mn} - \omega) = \partial_c \Theta(\omega_{mn} - \omega)$. Next, we obtain

$$\sigma_{\text{inj}}^{c;ab} = -\tau \frac{2\pi e^3}{\hbar^2} \int_{\omega_{cv}=\omega} \frac{d^{d-1}k}{(2\pi)^d} (\hat{n} \cdot \hat{c}) Q_{ba} \qquad (18)$$

for $\omega > 0$, where $\hbar\omega_{cv}$ is the energy gap between the conduction and valence bands, $\hat{n}$ is the surface normal vector, and

$$Q_{ba} = \sum_{n\in\text{occ}} \sum_{m\in\text{unocc}} r_{nm}^b r_{mn}^a$$

$$= \sum_{i,j} \partial_b f_i \partial_a f_j \frac{d_M(\delta_{ij} - \hat{f}_i\hat{f}_j + iJ_{ij})}{8f^2} \qquad (19)$$

is the so-called quantum geometric tensor [59] (see Appendix G for a derivation of the second equality). Here, $f = \sqrt{\sum_{i=1} f_i^2}$, and $J_{ij} = -i\sum_k \epsilon_{ijk}\hat{f}_k$ for $d_M = 2$ and $J_{ij} = 0$ for $d_M = 4$. The vanishing of J_{ij} for $d_M = 4$ is due to the presence of PT symmetry. Note that Q_{ba} is called the quantum geometric tensor because its real and imaginary parts are related to the quantum metric g_{ba} and the Berry curvature F_{ba} by

$$Q_{ba} = g_{ba} - \frac{i}{2} F_{ba}. \qquad (20)$$

The relationship between the circular injection current and the Berry curvature was found in Ref. [5]. On the other hand, the role of the quantum metric in determining the linear injection current was not discussed in the literature. We explain more on the geometric meaning of the quantum geometric tensor in Sec. IV B.

The shift current has a more complicated form, and it can be related to the matrix elements of the derivatives of the Hamiltonian as [60]

$$R_{mn}^{c,a} r_{nm}^b r_{mn}^a = i\frac{v_{nm}^b}{\omega_{mn}^2} \left[w_{mn}^{ac} - \frac{v_{mn}^c \Delta_{mn}^a + v_{mn}^a \Delta_{mn}^c}{\omega_{mn}} \right]$$

$$+ \frac{v_{nm}^b}{\omega_{mn}^2} \sum_{\omega_p \neq \omega_m, \omega_n} \left(\frac{v_{mp}^c v_{pn}^a}{\omega_{mp}} - \frac{v_{mp}^a v_{pn}^c}{\omega_{pn}} \right), \qquad (21)$$

where $w_{mn}^{ac} = \hbar^{-1}\langle m|\partial_a\partial_c H|n\rangle$ is the diamagnetic term. The second line involves virtual transitions among three

different bands, so it vanishes in our Dirac system, which only has two energy levels, with energy $\hbar\omega_c = f_0 + f$ and $\hbar\omega_v = f_0 - f$, where $f = \sqrt{\sum_{i=1} f_i^2}$. It then follows that [61]

$$\sigma_{\text{shift}}^{c;ab}(\omega) = -i\frac{2\pi e^3}{\hbar^2} \int_{\mathbf{k}} f_{vc}^{\text{FD}} C_{bca} \delta(\omega_{cv} - \omega) \qquad (22)$$

for $\omega > 0$, where

$$C_{bca} = -i\sum_{n\in\text{occ}} \sum_{m\in\text{unocc}} R_{mn}^{c,a} r_{nm}^b r_{mn}^a$$

$$= \frac{d_M}{8f^2} \sum_{i,j} (\delta_{ij} - \hat{f}_i\hat{f}_j + iJ_{ij})$$

$$\times \left[\partial_b f^i \partial_a \partial_c f^j - \frac{1}{f}(\partial_b f^i \partial_c f^j \partial_a f + \partial_b f^i \partial_a f^j \partial_c f) \right].$$
$$(23)$$

A special case of this formula was derived in Ref. [60] for two-band models with time-reversal symmetry. Our formula in Eq. (23) extends the existing formula to describe arbitrary systems described by the Dirac Hamiltonian in Eq. (17). We show below that C_{bca} has geometric meaning as a connection.

B. Geometry on the generalized Bloch sphere

Let us explain the geometric meaning of the quantum geometric tensor Q_{ba} as geometric quantities defined on the generalized Bloch sphere. This point of view is helpful for understanding the geometric meaning of C_{bca} as well as that of Q_{ba}.

We consider the following general Dirac Hamiltonian in Eq. (17). Then, the generalized Bloch vector $\mathbf{f}(\mathbf{k})$ is a map,

$$\mathbf{f}: \ \mathbf{BZ} \to \mathbb{R}^{\mathbf{d_\Gamma}}, \qquad (24)$$

where d_Γ is the number of Gamma matrices. This map defines a pullback of the quantum geometric tensor from the $\mathbf{f}$ space to the Brillouin zone.

Let us recall that the quantum geometric tensor has the following form:

$$Q_{ab} = \sum_{i,j} \partial_a f_i \partial_b f_j q_{ij}, \qquad (25)$$

where

$$q_{ij} = \frac{d_M(\delta_{ij} - \hat{f}_i\hat{f}_j + iJ_{ij})}{8f^2}, \qquad (26)$$

and $f = |\mathbf{f}|$. This form is a pullback of the quantum geometric tensor q_{ij} defined in the $\mathbf{f}$ space to the momentum space by a transformation $\partial_a f_i$ of tangent vectors

$$\partial_a = (\partial_a f_i)\partial_i, \tag{27}$$

where $\partial_i = \partial/\partial f_i$. The quantum metric and the Berry curvature are given by

$$g_{ab} = \sum_{i,j} \partial_a f_i \partial_b f_j \eta_{ij},$$

$$\frac{1}{2} F_{ab} = \sum_{i,j} \partial_a f_i \partial_b f_j \epsilon_{ij}, \tag{28}$$

where η_{ij} and ϵ_{ij} are the real and imaginary parts of q_{ij}, i.e., $q_{ij} = \eta_{ij} - i\epsilon_{ij}$. In this viewpoint, the quantum metric and the Berry curvature are pullbacks of the metric η_{ij} and the symplectic form ϵ_{ij} defined on the Bloch sphere. The metric η_{ij} measures length ds through $ds^2 = \eta_{ij} df^i df^j$, and the symplectic form ϵ_{ij} measures the oriented area dA through $dA = \epsilon_{ij} dx^i dx^j$ in the **f** space.

While the geometric quantity η_{ij} is defined on the whole **f** space, it can be regarded to measure the length on the unit sphere with $f = 1$, and it is irrelevant for the radial direction $f = |\mathbf{f}|$ [62]. For example, $ds^2 = (1/4)(d\theta^2 + \sin^2\theta d\phi^2)$ in polar coordinates when $d_M = 2$. To see this example without a coordinate transformation, first note that $P_{ij} = \delta_{ij} - \hat{f}_i\hat{f}_j$ is the projection to the plane perpendicular to $\hat{f}$. The metric measures the length only along the angular directions on a sphere with a fixed f. Also, the f^{-2} factor normalizes the length such that only the angle between two points on a sphere is measured. Similarly, the symplectic form also measures the area on the unit sphere. In this sense, the quantum geometric tensor is a geometric quantity defined on the generalized Bloch sphere ($f = 1$).

Another geometric quantity, called the Levi-Civita connection, can also be constructed on the generalized Bloch sphere. Its components are called the Christoffel symbols, and they can be written in two ways—the first and the second kinds. The Christoffel symbols of the second kind γ_{ij}^k are defined by

$$\partial_i \mathbf{e}_j = \sum_k \gamma_{ij}^k \mathbf{e}_k, \tag{29}$$

where $\mathbf{e}_i$ is the projection of the unit vector along the f_i direction to the tangent space by $P_{ij} = \delta_{ij} - \hat{f}_i\hat{f}_j$. It measures how vectors and tensors change as we move them parallel to the direction of the curved surface (which is the generalized Bloch sphere in our case). [64] We have

$$\gamma_{ij}^k = -\frac{f_i}{f^2}(\delta_{jk} - \hat{f}_j\hat{f}_k) - \frac{f_j}{f^2}(\delta_{ik} - \hat{f}_i\hat{f}_k). \tag{30}$$

It is related to the metric tensor η_{ij} by

$$\gamma_{ij}^k \equiv \sum_l (\eta^{-1})^{kl}\frac{1}{2}(\partial_i \eta_{jl} + \partial_j \eta_{il} - \partial_l \eta_{ij}), \tag{31}$$

where $(\eta^{-1}\eta)_{ij} = \delta_{ij} - \hat{f}_i\hat{f}_j$. Using the Christoffel symbols of the second kind and the quantum metric tensor, we define the Christoffel symbols of the first kind as

$$\gamma_{kij} \equiv \sum_l \eta_{kl}\gamma_{ij}^l$$

$$= -\frac{f_i}{f^2}\eta_{kj} - \frac{f_j}{f^2}\eta_{ki}. \tag{32}$$

Here, we distinguish the first and second Christoffel symbols by the uppercase and lowercase letters for the first component, while we do not distinguish the uppercase and lowercase letters for other quantities. We can also define a similar quantity using the symplectic form rather than the metric tensor by [65]

$$\tilde{\gamma}_{kij} \equiv \sum_l \epsilon_{kl}\gamma_{ij}^l$$

$$= -\frac{f_i}{f^2}\epsilon_{kj} - \frac{f_j}{f^2}\epsilon_{ki}. \tag{33}$$

To write γ_{kij} and $\tilde{\gamma}_{kij}$ in a unified way, we introduce

$$c_{kij} = \gamma_{kij} - i\tilde{\gamma}_{kij}. \tag{34}$$

We call c_{kij} the quantum geometric connection, in analogy with the quantum geometric tensor.

The Levi-Civita connection does not transform like a tensor under coordinate transformations [66], which is due to the derivative acting on tensorial quantities in the definition of the Christoffel symbols of the second kind [see Eq. (29)]. The Christoffel symbols of the second kind defined on the generalized Bloch sphere γ_{ij}^k are related to those defined in the Brillouin zone Γ_{ab}^c by $\Gamma_{ab}^c = \sum_d (g^{-1})^{cd}\frac{1}{2}(\partial_b g_{da} + \partial_a g_{db} - \partial_d g_{ab}) = \sum_{i,j,l}\partial_l k^c \partial_a f_i \partial_b \times f_j \gamma_{ij}^l + \sum_{i,j}\partial_i k^c \partial_a \partial_b f_j \delta_{ij}$, where the second term shows the nontensorial transformation property. It follows that the quantum geometric connection in the Brillouin zone has the form

$$C_{cab} = \sum_{i,j,k}\partial_c f_k \partial_a f_i \partial_b f_j c_{kij} + \sum_{ij}\partial_c f_i \partial_a \partial_b f_j q_{ij}, \tag{35}$$

where $C_{cab} = Q_{cd}\Gamma_{ab}^d$. It is identical to the quantity defined in Eq. (23), as one can see by using $\partial_a f = \sum_k f^{-1} f_k \partial_a f_k$. This quantity—the quantum geometric connection— reveals the geometric nature of the low-frequency shift current in the most transparent way. Let us note that, in general relativity, the equivalence principle requires that the Levi-Civita connection does not appear directly as an observable quantity because it is not invariant under a

coordinate transformation. However, here we do not have such an equivalence principle for the Bloch vector $\mathbf{f}$, so we can observe the Levi-Civita connection (or quantum geometric connection).

C. More on the geometric aspect of the shift current

Equation (22) shows that the linear (circular) shift current corresponds to the imaginary (real) part of the quantum geometric connection. Thus, the circular shift current reveals the Christoffel symbol of the first kind $\Gamma_{cab} = \frac{1}{2}(\partial_b g_{ca} + \partial_a g_{cb} - \partial_c g_{ab})$. On the other hand, the linear shift current is related to the Berry curvature as well as the quantum metric (through the Christoffel symbols of the second kind). Combined with the geometric property of the injection current in Eq. (18), it shows that PT-symmetric responses originate from the quantum metric only and that T-symmetric responses are controlled by both the Berry curvature and the quantum metric. When the diamagnetic term w_{mn}^{ac} in Eq. (E7) vanishes, the relation between the shift conductivity and the quantum metric and Berry curvature can be made more direct from

$$\sigma_{\text{shift}}^{c;ab} = -\frac{i}{\omega}\frac{2\pi e^3}{\hbar^2}\int_{\omega_{cv}=\omega}\frac{d^{d-1}k}{(2\pi)^d}[(\hat{n}\cdot\hat{a})Q_{bc} - (\hat{n}\cdot\hat{b})Q_{ac}^*]$$

(36)

for $\omega > 0$, when the diamagnetic term vanishes. This formula can be applied, e.g., to Dirac and Weyl Hamiltonians that are, at most, linear in momentum. Note that the real and imaginary parts of the conductivity in Eq. (36) have the form of the Berry curvature dipole [67] and the quantum metric dipole [68], respectively.

D. Generalization to multibands

Let us discuss generalizing our geometric interpretation to include three or more bands (when bands are doubly degenerate due to PT symmetry, this means that we consider six or more bands). The shift and injection conductivity takes the form $\sum_{n\in\text{occ}}\sum_{m\in\text{unocc}}\int_{\mathbf{k}}I_{nm}^{c;ab}\delta(\omega - \omega_{mn})$ for $\omega > 0$. Because the energy conservation imposed by the delta function chooses a particular set of unoccupied bands m for an occupied band n, the interband-transitive optical response is, in general, not associated with a property of the occupied band alone. On the other hand, for example, the quantum geometric tensor Q_{ba} is defined by summing over all occupied n and unoccupied m indices of the matrix elements by $\sum_{n\in\text{occ}}\sum_{m\in\text{unocc}}r_{nm}^b r_{mn}^a$, so it becomes a property of the ground state $\sum_{n\in\text{occ}}\sum_{m\in\text{all}}r_{nm}^b r_{mn}^a - \sum_{n\in\text{occ}}\sum_{m\in\text{occ}}r_{nm}^b r_{mn}^a$, depending only on the occupied states.

In our analysis, though, we focus on Dirac and Weyl points where the quantum geometric tensor diverges at the gap-closing points. Thus, the geometric quantities of the occupied bands are dominated by the property of the two

crossing bands $n = 1$ and $m = 2$, through a large value of $r_{12}^b r_{21}^a$ and their derivatives, and they manifest through the shift and injection currents for small ω. Similarly, when bands are Kramers degenerate due to PT symmetry, the matrix elements involving the indices for the four crossing bands are dominant contributions. Thus, at low frequencies, we have a good geometric approximation for the conductivity tensors by

$$\sigma_{\text{inj}}^{c;ab}(\omega) \approx -\tau\frac{2\pi e^3}{\hbar^2}\sum_{n,m}\int_{\mathbf{k}:\omega_{mn}=\omega}f_{nm}^{\text{FD}}(\hat{n}\cdot\hat{c})Q_{ba},$$

$$\sigma_{\text{shift}}^{c;ab}(\omega) \approx -i\frac{2\pi e^3}{\hbar^2}\int_{\mathbf{k}}\sum_{n,m}f_{nm}^{\text{FD}}C_{bca}\delta(\omega_{mn}-\omega),$$

(37)

where Q_{ba} and C_{bca} are the quantum geometric tensor and quantum geometric connection, respectively, defined by

$$Q_{ba} = \sum_{n\in\text{occ}}\sum_{m\in\text{unocc}}r_{nm}^b r_{mn}^a,$$

$$C_{bca} = \frac{1}{2}Q_{bd}(g^{-1})^{de}(\partial_c g_{ba} + \partial_a g_{bc} - \partial_b g_{ca}),$$

(38)

where $g_{ba} = \text{Re}[Q_{ba}]$ as above. In general, the injection conductivity tensors in Eq. (37) differ from the exact expression in Eq. (4) because the former has the information of all band indices rather than the specific bands n and m involved in the optical transition. Moreover, additional differences can be found in the shift conductivity tensors due to the virtual transition terms: $C_{bca} = -i\sum_{n\in\text{occ}}\sum_{m\in\text{unocc}}R_{mn}^{c,a}r_{nm}^b r_{mn}^a +$ virtual transitions (see Appendix I). When the optical excitation occurs very close to a gap-closing point, however, only the band indices near the gap closing significantly contribute to the geometric quantities, effectively selecting specific band indices. Also, virtual transition terms are suppressed by a factor $(\omega/\Delta E)^2$ [5], where ΔE is the characteristic energy difference between the crossing bands and the other bands. Thus, Eq. (37) becomes a good approximation near the gap closing. Let us note that, in two-band or PT-symmetric four-band models, Eq. (37) becomes exact and corresponds to Eqs. (18) and (22) above.

On the other hand, insulators or ordinary metals do not have geometric singularities, in general, and the geometric approximation Eq. (37) does not apply to them so well. Nevertheless, recalling that the Berry curvature of each band (rather than that of the whole occupied bands) is well defined, we can hope for the possibility of a well-defined geometric quantity associated with a pair of bands also. Let us see whether it makes sense to give a geometric meaning to the matrix element $r_{nm}^a r_{mn}^b \equiv g_{ab;nm} - iF_{ab;nm}/2$ by focusing on the real part $g_{ab;nm}$ (we note that it is different from the non-Abelian quantum metric [69,70] of the occupied bands, defined by $(g_{ab})_{n_1 n_2} = \sum_{m\in\text{unocc}}(r_{n_1 m}^a r_{mn_2}^b)$). Since $g_{ab;nm}$ is a positive-semidefinite symmetric rank-2 tensor,

i.e., $g_{aa;nm} \geq 0$ for all a for given n and m, this quantity is meaningful as a metric tensor, although its interpretation is not clear. This point of view can help us to understand the structure of the circular shift current. One can see that the matrix element of the circular shift current $R^{c,a}_{nm} r^b_{nm} r^a_{mn}$ can be written as $\Gamma_{bca;nm}$ + virtual transitions, where $\Gamma_{bca;nm}$ is the Christoffel symbol of the first kind defined by the metric $g_{ba;nm}$ (see Appendix I for a derivation). Therefore, one may still regard the shift current as originating from a Christoffel-symbol-like quantity, when the virtual transitions are negligible.

V. MODEL CALCULATIONS

Our theoretical analysis reveals the circular shift current as an interesting new component of the interband bulk photovoltaic response in magnetic systems. Also, the full generality of our theory allows us to understand the shift and injection currents in Dirac and Weyl semimetals in arbitrary spatial dimensions in a unified way. In this section, we investigate the shift and injection current responses of tilted Dirac and Weyl points more closely, with explicit calculations of the conductivity tensors. We first deal with massless Dirac and Weyl Hamiltonians up to linear order in momentum, which cover both type-I and type-II spectra in arbitrary spatial dimensions. In addition to the symmetry and divergence properties investigated above, we show the phenomenon of separation of responses, meaning that nonvanishing PT-symmetric responses and the T-symmetric responses do not coexist in the same component. This phenomenon can occur generically in tilted Dirac and Weyl systems having C_{2x} or $M_x T$ symmetry, where x is the direction of tilting. Next, we study a model of Dirac surface states of magnetic topological insulators, which includes k^2 and k^3 terms in the Hamiltonian.

A. Tilted Weyl and Dirac semimetals: k-linear order

Let us first revisit the model of a tilted Weyl point [13,25] to understand its general second-optical response in more detail. The Hamiltonian has the form

$$H_{\text{Weyl}} = -\mu - \hbar v' k_x + \hbar v(k_x \sigma_x + k_y \sigma_y + k_z \sigma_z). \quad (39)$$

The Weyl point described by this Hamiltonian is called type I when $|v'/v| < 1$ and type II when $|v'/v| > 1$ [58]. The spectra for the two cases are shown in Figs. 1(b) and 1(c). When light with frequency $\omega > 0$ is illuminated, optical excitation occurs when two bands have energy difference $\hbar\omega_{cv} = 2\hbar vk = \hbar\omega$ due to the energy conservation, and only the lower band is occupied, i.e., $\hbar\omega_v = -\mu + v'k\cos\theta - vk < 0$ and $\hbar\omega_c = -\mu + v'k\cos\theta + vk > 0$ (Fig. 1), where $k = |\mathbf{k}|$ and $k_x = k\cos\theta$. When $v' \neq 0$, the range of θ does not cover the whole sphere and is confined to a subspace $\theta_- < \theta < \theta_+$, in general (Fig. 1), where $\theta_\pm$ are functions of dimensionless parameters $2\mu/\hbar\omega$ and v'/v. The minimal angle θ_- is always zero for a type-I Weyl point, but it is typically nonzero for a type-II Weyl point [Figs. 1(d) and 1(e)]. This asymmetric excitation leads to a nonzero optical conductivity given by

$$\sigma^{c;ab}_{\text{shift}} = \frac{e^3}{2\pi\hbar^2}\frac{1}{\omega}\left(\frac{v}{\omega}\right)^{3-d}[\mathcal{F}^{c;ab}_{\text{shift}}(\theta_+) - \mathcal{F}^{c;ab}_{\text{shift}}(\theta_-)],$$

$$\sigma^{c;ab}_{\text{inj}} = \frac{e^3}{2\pi\hbar^2}\tau\left(\frac{v}{\omega}\right)^{3-d}[\mathcal{F}^{c;ab}_{\text{inj}}(\theta_+) - \mathcal{F}^{c;ab}_{\text{inj}}(\theta_-)]. \quad (40)$$

The forms of $\mathcal{F}^{c;ab}(\theta)$ for nonvanishing components are summarized in Table II. Because of the SO(2) rotational symmetry around the x axis, there are four independent components,

$$\sigma^{x;xx}_L, \quad \sigma^{x;yy}_L = \sigma^{x;zz}_L, \quad \sigma^{y;xy}_L = \sigma^{z;xz}_L, \quad \sigma^{y;zx}_L = -\sigma^{z;yx}_L \quad (41)$$

for the real component, and three independent components,

$$\sigma^{x;yz}_C, \qquad \sigma^{y;xy}_C = \sigma^{z;xz}_C, \qquad \sigma^{y;zx}_L = -\sigma^{z;yz}_C \quad (42)$$

for the imaginary component of the conductivity. Note that $\mathcal{F}^{c;ab}(\theta)$ follows the same symmetry. Remarkably, PT-symmetric responses (linear injection and circular shift) and T-symmetric responses (linear shift and circular injection) do not coexist in the same component. To understand this property, let us note that $PT = C_{2y} M_y T = C_{2z} M_z T$. Since our model has $C_{2y} T$ and $C_{2z} T$ symmetries, nonvanishing PT-symmetric responses appear in the components that are invariant under M_y and M_z, whereas T-symmetric responses appear in the components that reverse sign under M_y and M_z.

Figure 2 shows some representative components calculated from quantum geometric quantities by Eqs. (18), (19), and (36). There are some features that need to be discussed.

TABLE II. $\mathcal{F}^{c;ab}(\theta)$ of a single Weyl or Dirac point in two and three dimensions. Here, $0 \leq \theta \leq \pi$ is the absolute value of the polar angle from the x axis. The linear shift and circular injection parts vanish for a Dirac point because of PT symmetry.

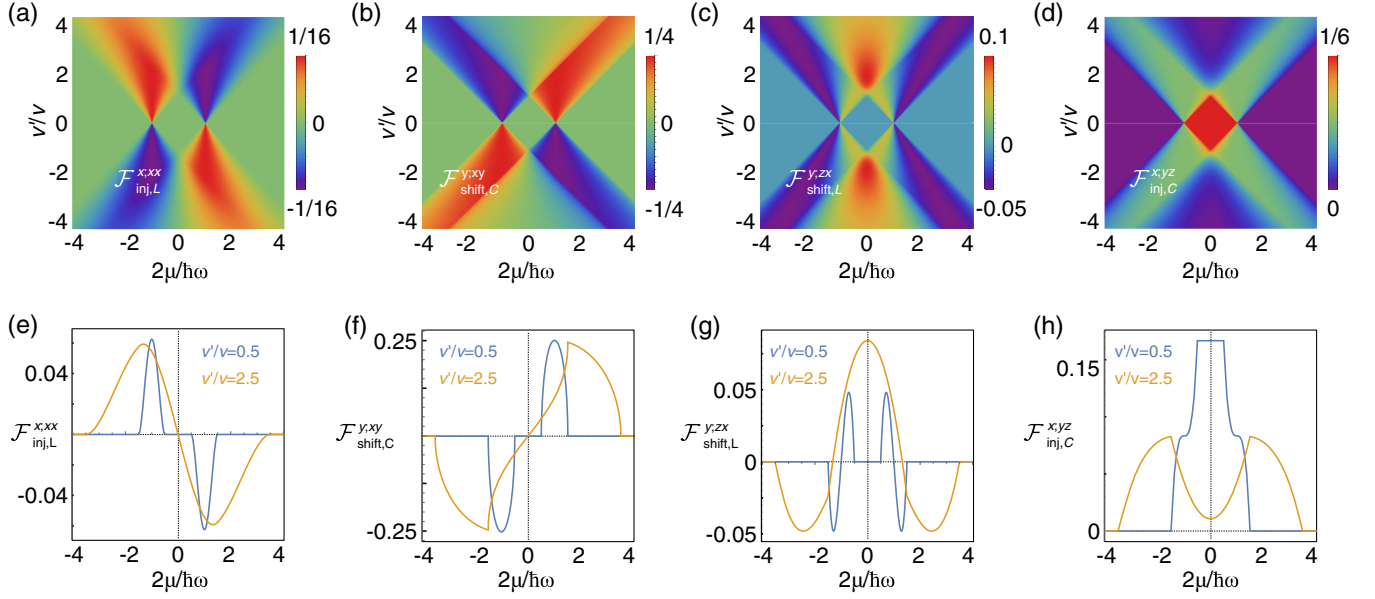| System	$\mathcal{F}^{x;xx}_{\text{inj},L}$	$\mathcal{F}^{x;yy}_{\text{inj},L}$	$\mathcal{F}^{y;xy}_{\text{inj},L}$	$\mathcal{F}^{y;xy}_{\text{shift},C}$	$\mathcal{F}^{y;zx}_{\text{shift},L}$	$\mathcal{F}^{x;yz}_{\text{inj},C}$	$\mathcal{F}^{y;zx}_{\text{inj},C}$
3D Weyl	$-\frac{1}{8}\cos^2\theta + \frac{1}{16}\cos^4\theta$	$-\frac{1}{16}\cos^2\theta - \frac{1}{32}\cos^4\theta$	$-\frac{1}{32}\sin^4\theta$	$-\frac{1}{4}\sin\theta$	$-\frac{1}{8}\cos\theta + \frac{1}{8}\cos^3\theta$	$-\frac{1}{12}\cos^3\theta$	$-\frac{1}{8}\cos\theta + \frac{1}{24}\cos^3\theta$
3D Dirac	$-\frac{1}{4}\cos^2\theta + \frac{1}{8}\cos^4\theta$	$-\frac{1}{8}\cos^2\theta - \frac{1}{16}\cos^4\theta$	$-\frac{1}{16}\sin^4\theta$	$-\frac{1}{2}\sin\theta$	0	0	0
2D Dirac	$\frac{1}{3}\sin^3\theta$	$\sin\theta - \frac{1}{3}\sin^3\theta$	$-\frac{1}{3}\sin^3\theta$	$-\sin\theta$	0	0	0

FIG. 2. $\mathcal{F}^{c;ab}$ of a tilted Weyl point in three dimensions. (a,e) $x;xx$ component of the linear injection. (b,f) $y;xy$ component of the circular shift. (c,g) $y;zx$ component of the linear shift. (d,h) $x;yz$ component of the circular injection. Since we take $\omega > 0$, the sign of $2\mu/\hbar\omega$ here should be understood as the sign of the chemical potential μ.

First, as we explained in Sec. III, only the circular injection current is nonvanishing at the neutral filling $\mu = 0$ in the type-I case where $|v'/v| < 1$. In this case, the Fermi surface is a point, so anisotropic excitation cannot occur. The circular injection response is quantized because of the quantized Berry curvature from a Weyl point, as found in Ref. [5] [see Eq. (18)]. Other responses are significant near $\hbar\omega = 2\mu$, where the anisotropic excitation occurs.

However, there are significant differences between the PT-symmetric responses and the linear shift response. The PT-symmetric responses have peaks at $\hbar\omega = |2\mu|$, i.e., when the excitation occurs on a full hemisphere, while T-symmetric responses vanish at $\hbar\omega = |2\mu|$ and change sign there [13]. For the linear injection current, the peak at $\hbar\omega = |2\mu|$ is natural because the transition of the electron velocity during the excitation from the valence band v to the conduction band c, $\Delta_{cv}^x = v_c^x - v_v^x$, is all positive or all negative on the hemisphere. There is no simple analogous way to understand the trend of the shift current response based on the shift vector, but the vanishing of the linear shift current response at $\hbar\omega = |2\mu|$ can be attributed to the T-symmetric nature. Since T symmetry requires that the current generated from one hemisphere is equal to the current generated from the other hemisphere, both hemispheres should generate zero currents because linear shift currents are not generated when excitations occur on the full sphere. There are also interesting differences between the PT-symmetric responses and T-symmetric responses at $\mu = 0$ in the type-II case where $|v'/v| > 1$. As explained in Sec. III, emergent CPT symmetry at $\mu = 0$ requires that the former has a vanishing response while the latter can have a

nontrivial response. In other words, PT-symmetric responses do not distinguish type-I and type-II cones at $\mu = 0$, whereas T-symmetric responses distinguish them.

As we understand a single Weyl point, it is straightforward to extend our knowledge to Dirac points in two and three dimensions. In both 2D and 3D, the protection of a Dirac point requires PT symmetry. In 2D, the Dirac Hamiltonian has the form $H_{2D} = -\mu - \hbar v' k_x + \hbar v(k_x \tau_x + k_y \tau_y)$, where $\tau_{i=x,y,z}$ are Pauli matrices for the orbital degrees of freedom, and spinless $PT = \sigma_z K$ symmetry forbids the mass term $m\sigma_z$. In 3D, the Dirac Hamiltonian has the form $H_{3D} = -\mu - \hbar v' k_x + \hbar v(k_x \tau_x + k_y \tau_y \sigma_x + k_z \tau_z)$, and the twofold degeneracy (Kramers degeneracy) of bands at every momentum requires $PT = i\sigma_y K$ symmetry. Here, $\tau_{i=x,y,z}$ and $\sigma_{i=x,y,z}$ are Pauli matrices for the orbital and spin degrees of freedom, respectively. In 3D, even in the presence of PT symmetry, two mass terms are allowed, which are $m_1 \tau_y \sigma_y$ and $m_2 \tau_y \sigma_z$. We need threefold or fourfold rotational symmetry to protect the Dirac point in 3D by disallowing mass terms. Our massless Dirac model has continuous θ rotational symmetry around the x axis under $C_\theta = e^{i\theta(\sigma_x + \tau_x \sigma_x/2)}$, satisfying $C_\theta H(\mathbf{k}) C_\theta^{-1} = H(C_\theta \mathbf{k})$. Keeping either threefold C_{3x} or fourfold C_{4x} rotational symmetry in crystals preserves the gap closing [54,71,72], which we assume here. Because gapless Dirac points have PT symmetry, they can only have linear injection or circular shift current responses. These responses have the same pattern shown for a Weyl point.

Here, we emphasize again that while multiple responses coexist in magnetic Weyl and Dirac semimetals, each response occurs through different components of the

conductivity. This property helps us measure each response separately. In particular, it facilitates the measurement of the circular shift current in magnetic Dirac and Weyl semimetals. Table II and Eq. (7) show that the current generated along the y direction under the illumination of circularly polarized light propagating in the z direction is only the circular shift current. The photocurrent along the y direction should thus be identified with the circular shift current.

B. Dirac surface state

As an application to a more realistic model with **k**-nonlinear terms, we study the single Dirac surface state of magnetic topological insulators. Let us begin with the following effective Hamiltonian studied in Refs. [23,24]:

$$H = -\mu + \frac{\hbar^2 k^2}{2m} + \hbar v(k_x \sigma_y - k_y \sigma_x) + \Delta \sigma_y. \quad (43)$$

Here, $\Delta \neq 0$ is due to spin ordering along the y direction, and it breaks $M_x = i\sigma_x$, rotation $C_{2z} = -i\sigma_z$, and time-reversal $T = i\sigma_y K$ symmetries. Since this in-plane ordering preserves $C_{2z}T$ symmetry, it does not open the gap, and it just shifts the location of Dirac points by $-\Delta/\hbar v$ from the time-reversal-invariant momentum. The shifting tilts the Dirac cone because of the quadratic term: If we write $(k_x, k_y) = (-\Delta/\hbar v + q_x, q_y)$, the Hamiltonian has the form $H = -\mu - (\hbar\Delta/mv)q_x + \hbar v(q_x\sigma_y - q_y\sigma_x)$ up to linear order in q, which is studied above. Assuming C_{3z} symmetry of the nonmagnetic state, we add a hexagonal warping term in order to account for the crystalline symmetry of the real system,

$$h_{\text{warp}} = \lambda(k_x^3 - 3k_x k_y^2)\sigma_z. \quad (44)$$

This term breaks $M_y = i\sigma_y$ symmetry and $C_{2z}T$ symmetry, which are preserved by the spin ordering, so it opens a small band gap (about 0.8 meV for parameters given below). Since T and $C_{2z}T$ symmetries are both broken, all four types of shift and injection currents can be generated in this system. However, the residual M_xT symmetry imposes that the separation of responses remains exact: Nonvanishing components of the conductivity are $\sigma_{\text{shift,L}}^{y;xx}$, $\sigma_{\text{shift,L}}^{y;yy}$, $\sigma_{\text{shift,L}}^{x;xy}$ for the linear shift current, $\sigma_{\text{inj,L}}^{x;xx}$, $\sigma_{\text{inj,L}}^{x;yy}$, $\sigma_{\text{inj,L}}^{y;xy}$ for the linear injection current, $\sigma_{\text{shift,C}}^{y;xy}$ for the circular shift current, and $\sigma_{\text{inj,C}}^{x;xy}$ for the circular injection current.

For a numerical calculation, we take $\mu = 50$ meV, $m = 0.13m_e$ (where m_e is the free electron mass), $\hbar v = 2.5$ eV Å^{-1}, $\lambda = 250$ eV Å^{-3}, and $\hbar\tau^{-1} = 1$ meV and use Eqs. (18) and (22). Figure 3 show the calculated photoresponsivity $\kappa^{c;ab} = 2\sigma^{c;ab}/\epsilon_0 c$, which has the dimension of the photocurrent density per unit of intensity of light [60]. The peak value (occurring at $\hbar\omega \sim 2\mu = 100$ meV) of the linear injection part is the strongest, and the others are
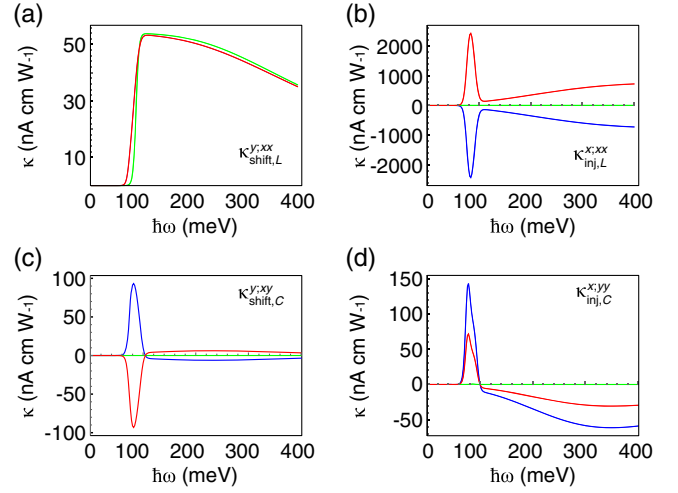

FIG. 3. Photoresponsivity of the magnetic Dirac surface state. Here, $\mu = 50$ meV, $m = 0.13m_e$, $\hbar v = 2.5$ eV Å^{-1}, $\lambda = 250$ eV Å^{-3}, and $\hbar\tau^{-1} = 1$ meV. Blue, green, and red curves correspond to $\Delta = 30$ meV, 0 meV, and -30 meV, respectively, and $\kappa^{c;ab} = 1$ nA cm W^{-1} is equivalent to $\sigma^{c;ab} = 1.33$ pA cm^{-1} V^{-2}.

smaller by 2 orders of magnitude. However, since the circular shift current grows as ω^{-2} while the linear injection current grows as ω^{-1}, the circular shift current can be comparable to or larger than the linear injection current when the peak is located below 10 meV. On the other hand, the small-frequency divergence of the linear shift current is weaker because it is due to $\lambda \neq 0$ [10] and is not from the tilting; thus, the peak value scales like $O(\omega^0)$ as μ is lowered. Therefore, the y-component photocurrent generated by a circularly polarized light, $j^y = (\kappa_{\text{shift,L}}^{yxx} + \kappa_{\text{shift,L}}^{yyy} - 2\kappa_{\text{shift,C}}^{y;xy})I$, is dominated by the circular shift ($\kappa_{\text{shift,C}}^{y;xy}$) current when $\hbar\omega \sim 2\mu < 100$ meV. The magnitude of the linear shift current and the circular shift current can be compared in experiments since the circular parts can be measured from the current difference between the left-circularly polarized light and the right-circularly polarized light.

In experiments, the value of the observed photocurrents can be smaller than the value predicted here. For example, the photocurrents observed in Ref. [24] show photoresponsivity of about 5 nA cm^{-1} W^{-1} at $\omega \sim 250$ meV, which is 2 orders of magnitude smaller than the calculated value here. While several factors can contribute to this reduction, one is from the cancellation between the top and bottom surfaces. This cancellation can be reduced by increasing the thickness of the sample because light attenuates more while propagating within the bulk such that the photocurrent is generated significantly on only one surface that is directly illuminated.

VI. FIRST-PRINCIPLES CALCULATIONS FOR REAL TOPOLOGICAL SEMIMETALS

For further demonstrations of our theory beyond simple two-band models, we perform first-principles calculations

on the shift and injection photocurrent conductivities as well as geometric quantities of antiferromagnetic MnGeO$_3$ and ferromagnetic PrGeAl, respectively, as representatives of real magnetic Dirac and Weyl semimetals. We notice that such calculations on the bulk photovoltaic effects in real magnetic topological semimetals have not been reported yet, despite the fact that topological semimetals are expected to be efficient infrared and terahertz photodetectors [1].

A. Antiferromagnetic Dirac semimetal MnGeO$_3$

MnGeO$_3$ forms a centrosymmetric rhombohedral structure [see Fig. 9(a)] with space group $R\bar{3}$ [73], and consequently, it does not exhibit any bulk photovoltaic effects. Interestingly, it becomes antiferromagnetic below 38 K [73], and the AF structure (magnetic space group $-3'$) [see Fig. 9(a)] breaks both T and P symmetries while preserving the combined PT symmetry [42], thus leading to AF-induced bulk photovoltaic effects with linear injection and circular shift currents (see Table I). Furthermore, it was recently predicted to be a Dirac semimetal with PT symmetry-protected Dirac points (DPs) [42].

In AF MnGeO$_3$, because of its PT symmetry, there are only nonvanishing circular shift photocurrents and linear injection photocurrents, as mentioned before (see Table I). Furthermore, the $-3'$ magnetic space group admits only three nonvanishing independent matrix elements (i.e., $xxz = -xzx = yzy$, $xyz = -xzy = -yxz$, and $zxy = -zyx$) of the circular shift conductivity tensor and six nonvanishing independent matrix elements (i.e., $xxx = -xyy = -yxy$, $xyz = -yxz$, $xxz = yyz$, $xxy = yxx = -yyy$, $zxx = zyy$, and zzz) of the linear injection conductivity tensor [53]. Hereafter, we use the shorthand notation cab for $\sigma^{c;ab}$. We display these nonvanishing conductivity elements in the low photon energy range in Fig. 4. For simplicity, we plot only the four pronounced xxx, xxz, zxx, and zzz elements of the linear injection conductivity tensor in Fig. 4. Here, $\hbar\tau^{-1} = 10$ meV is assumed. We notice that the magnitudes of the linear injection conductivity elements ($\sigma^{c;ab}$) are gigantic in the photon energies below 0.25 eV (Fig. 4). The magnitudes are of order $\tau e^3/(2\pi\hbar^2) = 500$ μA/V^2, which are 1 order of magnitude larger than those in archetypical polar semiconductors CdS and CdSe [74]. Circular shift photocurrents (Fig. 4) are also 10 times larger than linear shift currents in semiconductors CdS and CdSe [74]. This fact is remarkable because it demonstrates that the AF magnetism-induced linear injection and circular shift photocurrents, respectively, can be as large as circular injection and linear shift currents in nonmagnetic noncentrosymmetric materials. Furthermore, the photocurrents in AF semimetals can be controlled via manipulating the magnetism with, e.g., an applied magnetic field [26].

AF MnGeO$_3$ hosts at least three DPs near the Fermi level E_F along the k_z axis, as shown in Fig. 5. In particular, there is a DP just above E_F (at 1.7 meV), located close to the Γ
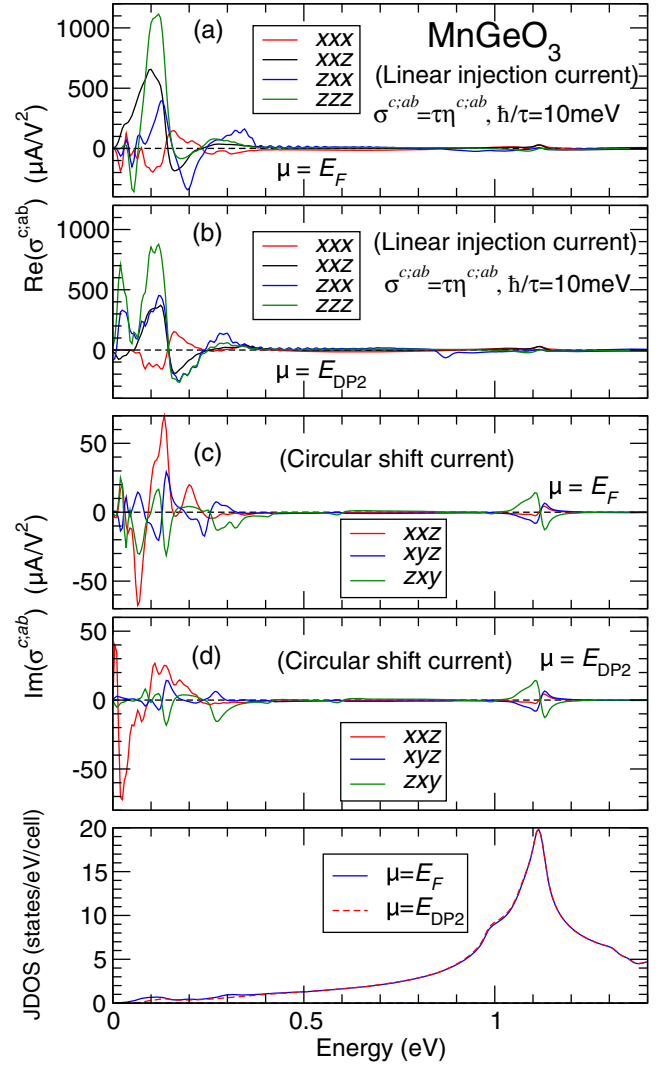

FIG. 4. Conductivity tensors and JDOS of antiferromagnetic MnGeO$_3$. (a,b) Linear injection. (c,d) Circular shift. In panels (b) and (d), the conductivities are calculated with the Fermi level set to the DP$_2$ Dirac point energy (see Fig. 5). (e) JDOS as a function of photon energy.

point [at $\mathbf{k}_{\text{DP1}} = (0, 0, -0.00364)2\pi/a$]. This DP could explain the large values of the calculated photocurrents, as shown in Figs. 4(a) and 4(c). To further examine the important contributions of the DPs to the photocurrents, we also calculate the conductivity spectra with the Fermi level set to the DP2 Dirac point energy (i.e., $E = 46.5$ meV). DP2 is located at $\mathbf{k}_{\text{DP1}} = (0, 0, 0.11112)2\pi/a$ above the $k_z = 0$ plane in the k space [see Fig. 5(a)]. We notice that both the shapes and magnitudes of all the conductivity spectra, except the conductivity element σ^{xxz}, roughly remain the same. For example, the gigantic peak of about 1000 μA/V^2 at about 100 meV in the Re(σ^{zzz}) linear injection current spectrum appears in both cases [see green curves in Figs. 4(a) and 4(b)]. Nonetheless, its sharp
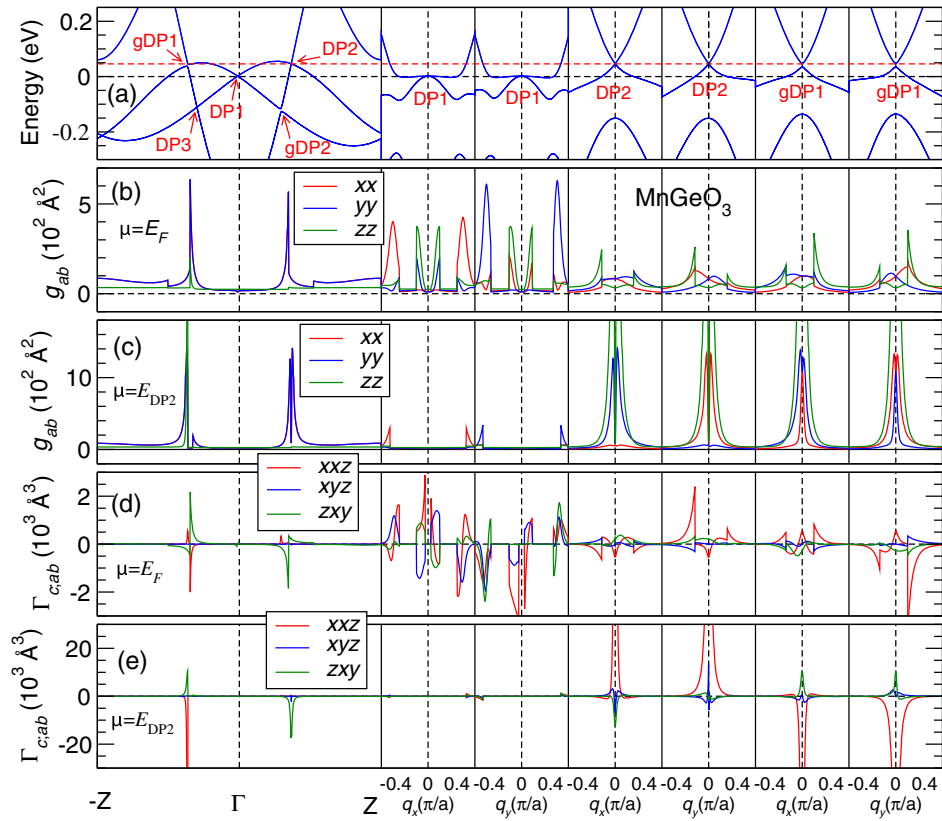
FIG. 5. Enhancement of geometric quantities near Dirac points. (a) Energy bands along the k_z axis from $-\pi/c$ to π/c ($Z = \pi/c$) and also along the k_x and k_y directions through the DP1 and DP2 Dirac points as well as the gDP1 gapped Dirac point. (b,c) Quantum metric (g_{ab}) along the same symmetry lines as in panel (a), calculated for the Fermi energy (E_F) and the DP2 energy (E_{DP2}), respectively. (d,e) Same as in panels (b) and (c), respectively, but for the Christoffel symbol of the first kind ($\Gamma_{c;ab}$). Here, $\mathbf{q} = \mathbf{k} - \mathbf{k}_{DP}$ denotes the momentum displacement from a DP (qDP) point.

negative peak at 50 meV disappears in the case where the chemical potential μ is tuned to $\mu = E_{DP2}$, and a sharp positive peak larger than 700 μA/V^2 occurs at 20 meV instead. Interestingly, there is a sharp positive peak at a photon energy of 5 meV in the Im(σ^{xxz}) circular shift current calculated by setting $\mu = E_{DP2}$. This peak is due to the ω^{-1} behavior of the shift conductivity near the Dirac point. Comparing the red curves in Figs. 1(c) and 1(d) for Im(σ^{xxz}), one can also see that the large negative peak moves from photon energy 65 meV to 25 meV [see Fig. 4(d)].

While an enhanced joint density of states (JDOS), $\rho(\omega) = \int_{\mathbf{k}} \sum_{m,n} f_{nm} \delta(\omega_{mn} - \omega)$, is a possible origin of large conductivity tensors in insulators [60], it cannot explain the peaks shown here. Figure 4(e) shows that the JDOS is suppressed at low frequencies rather than being enhanced. As we show above, linear injection and circular shift currents are, respectively, related to quantum metric (g_{ab}) and Christoffel symbols of the first kind ($\Gamma_{c;ab}$) at low energies through Eq. (37). Thus, the large enhancement of conductivity tensors has geometric origin. To demonstrate this origin, we display g_{ab} and $\Gamma_{c;ab}$ at $\mu = E_F$ and also at $\mu = E_{DP2}$ along the symmetry lines in Fig. 5. For most of

the DPs, a DP is associated with a gapped DP (gDP) located approximately at the inverted position in k space. For example, the associated gPD for DP2 is gDP1 at $\mathbf{k}_{DP1} = (0, 0, -0.11051)2\pi/a$, and the DP2 energy level falls within the gDP1 band gap [see Fig. 5(a)]. On the other hand, there is no gDP associated with DP1. Figures 5(b) and 5(d) clearly show that for $\mu = E_F$, g_{ab} and $\Gamma_{c;ab}$ have sharp peaks near DP1 along the k_x and k_y directions. Note that g_{xx} and g_{yy} also peak sharply at the positions of the DP2 and gDP1 along the k_z axis, even though $\mu = E_F \neq E_{DP2}$. This result indicates that the gigantic linear injection and circular shift currents stem, respectively, from the large values of the quantum metric and Christoffel symbol in the vicinity of the DP1 Dirac point. Furthermore, g_{zz} has prominent peaks in the vicinity of (but slightly away from) the DP2 and gDP1 points along the k_x and k_y directions, which are mainly caused by the interband transitions from the lower (occupied) Dirac cone to higher (empty) Dirac cone with transition energies of about 0.1 eV [see Fig. 5(b)]. These g_{zz} peaks thus give rise to the gigantic peak in the linear injection current Re(σ^{zzz}) at around 0.1 eV [see green curves in Fig. 4(a)].

For $\mu = E_{DP2}$, as expected, g_{ab} and $\Gamma_{c;ab}$ exhibit sharp peaks close to both the DP2 and gDP1 points [see Figs. 5(c) and 5(e)]. In particular, g_{zz} has huge positive peaks near the DP2 and gDP1 points along all three Cartesian coordinate directions, thus resulting in the prominent peak at 0.1 eV in linear injection conductivity $\text{Re}(\sigma^{zzz})$ [Fig. 4(b)], as in the $\mu = E_F$ case [Fig. 4(a)]. Nevertheless, Fig. 5(e) shows that the $\Gamma_{c;ab}$ peaks near the DP2 and gDP1 have opposite signs. This behavior could explain why the circular shift conductivity elements $\text{Im}(\sigma^{xyz})$ and $\text{Im}(\sigma^{zxy})$ become smaller when the Fermi level is raised from E_F to E_{DP2} [Figs. 4(c) and 4(d)] because the contributions from the DP2 and gDP1 cancel each other to some extent. In contrast, the linear injection current elements remain almost unchanged, mainly because the g_{ab} peaks have the same signs. Nonetheless, there is a huge peak in the Γ_{xxz} at gDP1, which is absent at DP2, because now the Fermi level falls within the gDP1 gap [see Fig. 5(e)]. This peak results in the large low-energy peaks in the $\text{Im}(\sigma^{xxz})$ conductivity element [see red curves in Fig. 4(d)].

B. Ferromagnetic Weyl semimetal PrGeAl

PrGeAl forms a body-centered tetragonal structure [see Fig. 9(b)] with noncentrosymmetric space group $I4_1md$ and point group $4mm$ [75]. It becomes ferromagnetic at $T_C = 16$ K [44], and the FM structure [Fig. 9(b)] has no T symmetry nor PT symmetry. Therefore, all four types of photocurrents may emerge in FM PrGeAl (Table I). Interestingly, it was recently predicted to be a rare ferromagnetic noncentrosymmetric Weyl semimetal [43]. Furthermore, the Weyl nodes and surface Fermi arcs in PrGeAl were observed in very recent photoemission spectroscopy experiments [44]. Thus, FM PrGeAl provides a valuable platform for studying all types of bulk photovoltaic effects in Weyl semimetals.

The crystalline point group of PrGeAl is $4mm$. Thus, there are three inequivalent nonvanishing matrix elements (i.e., $xxz = yyz$, $zxx = zyy$, and zzz) of linear shift conductivity and one nonvanishing element ($xxz = yyz = -xzx = -yzy$) of circular injection conductivity in PrGeAl above $T_C = 16$ K [53]. The magnetic point group of FM PrGeAl is $4m'm'$. Consequently, in addition, there are two nonvanishing elements (i.e., $xyz = -xzy = -yxz$ and $zxy = -zyx$) of circular shift conductivity and one nonvanishing element ($xyz = -yxz$) of linear injection conductivity in PrGeAl below T_C [53]. Here, the presence of M_xT and M_yT symmetries forbids linear shift and injection conductivities to be simultaneously nonvanishing in the same component. The same is true for the circular polarization. The calculated conductivity spectra of these nonvanishing matrix elements are displayed in Fig. 6. We notice that all the shift current elements have large peaks below a photon energy of 0.25 eV [see Figs. 6(a) and 6(b)]. These large peaks are due to the ω^{-1} enhancement of the shift conductivity tensors at low frequencies. Indeed, the magnitudes of these peaks below 0.1 eV are
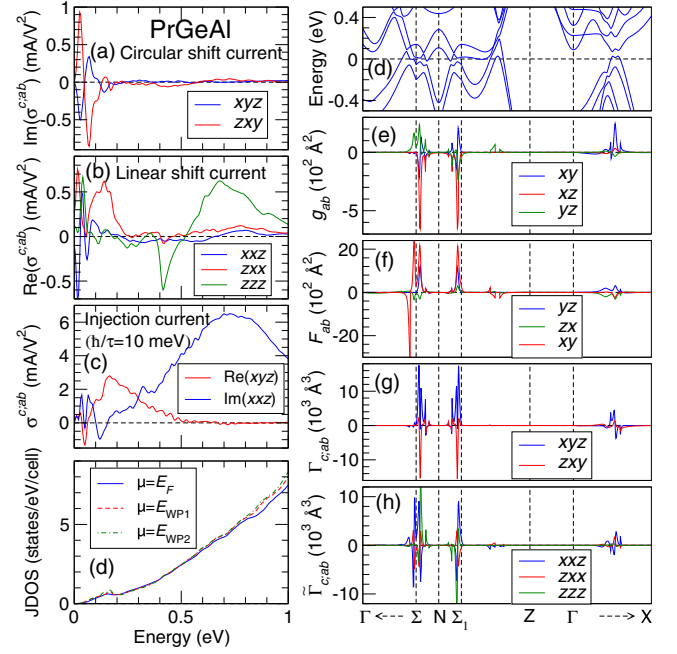

FIG. 6. Conductivity tensors and geometric quantities in ferromagnetic PrGeAl. (a,b) Shift and (c) injection conductivity tensors. (d) JDOS as a function of photon energy. The cases with $\mu = E_{WP1}$ and $\mu = E_{WP2}$ are also shown. (e) Energy bands, (f) quantum metric g_{ab}, (g) Berry curvature F_{ab}, (h) Christoffel symbol $\Gamma_{c;ab}$, and (i) symplectic Christoffel symbol $\tilde{\Gamma}_{c;ab}$ along the high-symmetry lines in the Brillouin zone [see Fig. 9(d) in Appendix K].

comparable to those in archetypical nonmagnetic Weyl semimetal TaAs [16], which also has the $I4_1md$ space group. The linear shift current element $\text{Re}(\sigma^{zzz})$ is also large in the higher energy range between 0.4 eV and 1.0 eV. This peak is not due to magnetic order because it is observed in T-symmetric responses. It is hardly related to the responses of Weyl points. The peak is far from the Fermi level; also, the conductivity components showing the large peaks are not generated by linearly dispersing Weyl points (see Table II, for example). We do not aim to explain its origin here. The calculated circular shift conductivity elements below 0.2 eV are comparable to that of the linear shift current (Fig. 6), and remarkably, they are 1 order of magnitude larger than those in the AF Dirac semimetal MnGeO$_3$ [see Figs. 4(c) and 4(d)]. No first-principles calculation of the circular shift current in other semimetals has been reported yet.

Similar to the linear shift conductivity, circular injection conductivity $\text{Im}(\sigma^{xyz})$ has a gigantic broad peak between 0.5 eV and 1.0 eV, and the peak value is almost 1 order of magnitude larger than that of linear injection conductivity in AF MnGeO$_3$ (see Fig. 4). It also has large peaks below 0.15 eV, although the magnitudes of these peaks are a few times smaller than the gigantic peak in the higher energy region. Linear injection conductivity $\text{Re}(\sigma^{xyz})$ in FM PrGeAl is also large and is about 10 times larger than that of AF MnGeO$_3$ in the very-low-energy region. This 1-

order-of-magnitude enhancement can be related to the presence of many Weyl points, as we analyze further below.

As in MnGeO$_3$, JDOS is suppressed at low energies [Fig. 6(d)]. Thus, the origin of the large low-frequency photocurrents should be attributed to the geometric enhancement. We have calculated all four geometric quantities along the symmetry lines in the Brillouin zone [Fig. 9(d)], as displayed in Fig. 6. We find that all four quantities have sharp peaks in the vicinity of the Σ and Σ_1 points, where there are several anticrossing nodal points, with the Fermi level falling within their gaps [see Fig. 6(e)]. Since these gaps near the anticrossing points are mostly within 0.1 eV, the large peaks in the geometric quantities thus give rise to the sharp photoconductivity peaks around 0.1 eV and below. In particular, Christoffel symbols Γ_{xyz} and Γ_{zxy} have gigantic peaks near the Σ and Σ_1 points with the same signs, thus resulting in sharp peaks in circular shift conductivities $\mathrm{Im}(\sigma^{xyz})$ and (σ^{zxy}), respectively, below a photon energy of 0.1 eV [Fig. 6(a)].

FM PrGeAl has been reported to be a rare noncentrosymmetric FM Weyl semimetal with at least 160 WPs within ± 0.1 eV of the Fermi level [43]. Furthermore, there are both type-I and type-II WPs among them. Here, we consider two WPs, one type I and the other type II, and study their influences on the photocurrents. The type-I WP (WP1) sits at $\mathbf{k} = (0.160, 0.204, -0.003)2\pi/a$ in the BZ and is located at 53.9 meV above E_F (E_{WP1}). The type-II WP (WP2) is at $\mathbf{k} = (0.015, 0.255, 0.217)2\pi/a$, and its energy is 67.4 meV above E_F (E_{WP2}). They correspond, respectively, to Weyl points W_3^1 and W_2^1 reported in Ref. [43]. To study the influences of the WPs on the photocurrents, we calculate all the nonvanishing conductivity elements and all the geometric quantities with the Fermi level set to E_{WP1} and also to E_{WP2}.

The conductivity and geometric quantity spectra obtained by setting the Fermi level to the WP1 energy (E_{WP1}) are plotted in Fig. 7. Remarkably, compared with the $\mu = E_F$ case in Fig. 6, all the photoconductivity elements within the photon energy of 50 meV increase by a factor of 2 or more. In particular, the linear shift conductivity element $\mathrm{Re}(\sigma^{zxx})$ is enhanced by a factor of 5 [Fig. 7(b)]. Other changes include that the peak at about 70 meV in circular shift conductivity elements $\mathrm{Im}(\sigma^{xyz})$ and $\mathrm{Im}(\sigma^{zxy})$ is significantly reduced [Fig. 7(a)] and that the positive peak at about 40 meV in linear shift conductivity element $\mathrm{Re}(\sigma^{zzz})$ changes to a negative peak [Fig. 7(a)]. Nonetheless, the features of all the conductivity elements above 100 meV remain essentially unchanged.

The changes caused by moving the Fermi level to the WP1 energy mentioned above can be largely explained by the distributions of the four geometric quantities in the vicinity of the WP1, as displayed in Figs. 7(e)–7(h). For example, the symplectic Christoffel symbol $\tilde{\Gamma}_{zxx}$ has high positive peaks along all three coordinate directions near the WP1 [see Fig. 7 (h)]. These peaks thus give rise to the fivefold increased
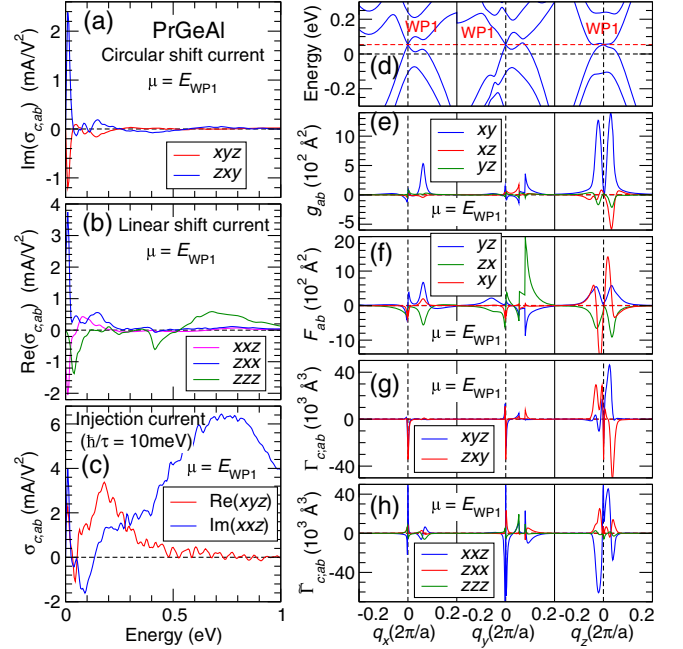

FIG. 7. Same as in Fig. 6, but with $\mu = E_{\mathrm{WP1}}$. (a,b) Shift and (c) injection conductivity tensors. (d) Energy bands, (e) quantum metric g_{ab}, (f) Berry curvature F_{ab}, (g) Christoffel symbol $\Gamma_{c;ab}$, and (h) symplectic Christoffel symbol $\tilde{\Gamma}_{c;ab}$ along the three Cartesian coordinate axis directions through the WP1 ($E = E_{\mathrm{WP1}}$). Here, $\mathbf{q} = \mathbf{k} - \mathbf{k}_{\mathrm{WP1}}$ denotes the momentum displacement from the WP1.

linear shift conductivity $\mathrm{Re}(\sigma^{zxx})$. Note that although in the $\mu = E_F$ case $\tilde{\Gamma}_{zxx}$ also has sharp peaks near the Σ and Σ_1 points, these peaks have both positive and negative signs [see Fig. 6(i)], and thus their contributions to the linear shift conductivity cancel each other to some extent.

The results obtained by setting the Fermi level to the energy of the type-II WP2 are plotted in Fig. 8. We notice that, as in the WP1 case, all the photoconductivity spectra remain more or less unchanged for photon energies larger than 100 meV. As for the WP1 case, the peak height of linear shift conductivity $\mathrm{Re}(\sigma^{zxx})$ at a very low energy of about 10 meV gets doubled, although the sign of the peak changes from positive to negative [see Fig. 8(b)]. However, in contrast to the WP1 case, many low-energy peaks, especially of shift current conductivity elements, become smaller [Figs. 8(a) and 8(b)]. In particular, the peak at 10 meV in both circular shift elements $\mathrm{Im}(\sigma^{xyz})$ and $\mathrm{Im}(\sigma^{zxy})$ decreases by a factor of nearly 2, and also the peak sign changes to the opposite sign. These different changes in the low-energy photoconductivity spectra between the type-I and type-II Weyl-point cases may be attributed to their different energy dispersions and hence the different distributions of the four geometric quantities near the Weyl points (see Figs. 7 and 8). Figure 7(d) shows that in the type-I WP1 case, the upper and lower Weyl cone bands lie, respectively, above and below the WP1 energy.
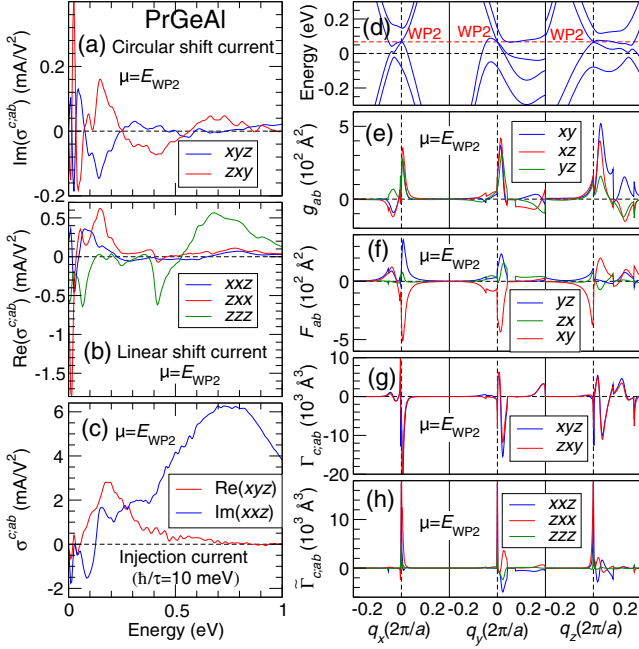
FIG. 8. Same as in Fig. 6, but with $\mu = E_{WP2}$. (a,b) Shift and (c) injection conductivity tensors. (d) Energy bands, (e) quantum metric g_{ab}, (f) Berry curvature F_{ab}, (g) Christoffel symbol $\Gamma_{c;ab}$, and (h) symplectic Christoffel symbol $\tilde{\Gamma}_{c;ab}$ along the three Cartesian coordinate axis directions through the WP2 $E = E_{WP2}$. Here, $\mathbf{q} = \mathbf{k} - \mathbf{k}_{WP2}$ denotes the momentum displacement from the WP2.

As a result, the low-energy inter-Weyl-band transitions may occur in all three coordinate directions when the Fermi level is set to E_{WP1}. This can result in large peaks in the four geometric quantities near the WP1, thus leading to the many-fold enhancements in photocurrents, as discussed above. In the type-II WP2 case, in contrast, both upper and lower Weyl bands along the $-k_x$ and $+k_y$ directions lie below E_{WP2} [see Fig. 8(d)]. This hinders the low-energy inter-Weyl-band transitions along these two directions when E_F is set to E_{WP2} and thus reduces the peaks in the geometric quantities near the WP2, thereby leading to several smaller peaks in the photocurrents below about 20 meV. Of course, in a real topological semimetal such as in the present system, the situation could be more complicated. Figure 8(d) shows that other bands may come quite close to the WP2 in energy; thus, they enable, e.g., the transitions from two Weyl bands below E_{WP2} to the other bands above E_{WP2} along the $-k_x$ and $+k_y$ directions, also giving rise to prominent peaks in the geometric quantities near the WP2 [see Figs. 8(e)–8(h)].

VII. DISCUSSION

Let us discuss some issues related to the smallness of the frequency. We note that our theory is reliable for the photon frequency above 1 THz because we assume $\omega \gg \Gamma$. Since the typical relaxation time in semimetals is 1 picosecond,

$\omega/2\pi > 1$ THz should be taken for our theory to apply. Thus, the divergence of the responses in our model should not be interpreted as a physical divergence, and it is cut off at $\omega \sim \Gamma$. Moreover, intraband (i.e., nontransitive) second-order optical responses exist in magnetic systems, and they become comparable to the interband responses when $\omega \lesssim \Gamma$. To estimate the magnitude of the intraband responses, let us consider the semiclassical second-order optical response $\sigma_{SC}^{c;ab}(\omega) = -(e^3/\hbar^2)(\omega^2 + \Gamma^2)^{-1} \times \sum_n \int_{\mathbf{k}} f_n^{FD} \partial_a \partial_b v_n^c$. It has the same symmetry property as the linear injection current (so it appears in magnetic systems where time-reversal symmetry is broken) and scales as $\omega^{-2}\mu^{2-d}$ near tilted Dirac or Weyl points. Since the ω^{-2} factor enhances the semiclassical response at low frequencies, it becomes comparable to the peak value of the linear injection response at $\omega \lesssim \tau^{-1} = \Gamma$ if we take $\mu \sim \omega$.

Another issue at low frequencies is the validity of perturbation theory. We suppose that the photovoltaic responses are dominated by the second-order responses since the electric field is generally weak enough. However, at small frequencies, $A = E/\omega$ becomes large, so higher-order responses can become significant. According to the Floquet theory analysis in Ref. [4], perturbation theory works well for $|\omega^{-1}eEv| \ll \hbar\Gamma$, where we assume that the interband velocity matrix element has the same order of magnitude as the intraband velocity. It sets a lower bound for ω. For $\hbar v \sim 1$ eV Å^{-1} and $\Gamma \sim 1$ THz, the lower bound is $\omega_{min} \approx \sqrt{I/(W/cm^2)}$THz. While this bound is very small for typical lasers with intensity $I < 1$ W/cm^2, it should be taken into account for an analysis of the experimental results obtained by using high-intensity pulse lasers.

In the nonperturbative regime, light absorption occurs faster than the interband relaxation, so electrons are excited until the system reaches a new equilibrium where the absorption and emission of light find a balance. The relaxation plays an important role here because a mismatch between the absorption and emission, which generate opposite photocurrents, requires a finite relaxation [4]. Even in a very clean system with an extremely small Γ, the low-frequency divergent behavior we discuss above is cut off because of this reason.

At finite temperature, thermal fluctuation can significantly reduce low-frequency photovoltaic response in tilted-Dirac or Weyl semimetals [13]. When the peak value is considered, the relevant frequency scale where the peak value is reduced to half is $2|v/v'|k_BT/\hbar$ for type I and $2k_BT/\hbar$ for type II. It sets a quite-high lower bound since $2k_BT/\hbar = 12$ THz at room temperature (cf. 0.17 THz at 4.2K and 3.2 THz at 77 K). When the tilting is small such that $|v'/v| < 0.4$, the cutoff scale is larger than 30 THz at room temperature, which is the highest edge of the terahertz radiation. Therefore, cooling will be needed in order for tilted-Dirac or Weyl semimetals to work as an efficient terahertz photodetector.

Throughout this work, we focused on the dc generation. However, let us note that our results can also be applied to the second harmonic generation, where an alternating current of frequency 2ω is generated by a uniform illumination of light with frequency ω. Since the second harmonic generation is associated with the shift vector [4,13], its low-energy divergence has the same form as that for the shift current [13], and thus it can be related to the quantum geometric connection. We believe that similar geometric interpretations of other quantities are also possible. It will be an interesting topic to explore quantum geometric properties of the third-order optical conductivity. Since it has four components, we expect the existence of a third-order optical response controlled by the Riemann curvature tensor $R^a_{bcd} = \partial_c\Gamma^a_{db} - \partial_d\Gamma^a_{cb} + \sum_e(\Gamma^a_{ce}\Gamma^e_{db} - \Gamma^a_{de}\Gamma^e_{cb})$.

ACKNOWLEDGMENTS

Note added.—Recently, Hikaru Watanabe and Yoichi Yanase studied the bulk photovoltaic responses in magnetic systems independently of ours [76]. They also figured out the circular shift current and discussed its enhancement near gap-closing points. Our results are consistent with the results in their preprint when there is an overlap.

Note added in proof.—The conclusion of a somewhat ad hoc discussion in the paragraph containing Appendix Eq. (E8) can be justified by fully taking the degeneracy into account. For this purpose, we need to write the generalized derivative in Eq. (E3) with the U(N) Berry connection, instead of the U(1) Berry r^c_{mm} and r^c_{nn}. See Ref. [76]. Then, the virtual transition terms in Eq. (E7) appears as the sum over non-degenerate states ($\omega_p \neq \omega_n, \omega_m$).

APPENDIX A: FREQUENTLY USED IDENTITIES

In this Appendix, we use the following two identities:

$$
\begin{aligned}
\langle m|\partial_a O|n\rangle &= \partial_a O_{mn} - i(r^a_{mp}O_{pn} - O_{mp}r^a_{pn}) \\
&= \partial_a O_{mn} - i[r^a, O]_{mn},
\end{aligned} \tag{A1}
$$

where we integrate by parts in the first line. The following is a specific example of the above identity with $O = H/\hbar$, and it is used very often in the subsequent Appendixes:

$$
\begin{aligned}
v^a_{mm} &= \partial_a\omega_m, \\
v^a_{mn} &= i\omega_{mn}r^a_{mn} \quad (m \neq n).
\end{aligned} \tag{A2}
$$

APPENDIX B: SHIFT AND INJECTION CURRENTS FROM THE FERMI GOLDEN RULE

Let us derive the expression of the shift and injection currents from the Fermi golden rule. Here, we drop the light polarization dependence of the shift vector. Since $\mathbf{E}(t) = E(\omega)e^{-i\omega t} + E(-\omega)e^{i\omega t}$, where $E(-\omega) = E(\omega)^*$, both the ω and $-\omega$ components contribute:

$$
\begin{aligned}
j^c_{\text{shift}} &= \int_{\mathbf{k}} \sum_{\substack{n\in\text{occ}\\m\in\text{unocc}}} (-eR^c_{mn})f^{\text{FD}}_{nm}\mathcal{M}_{m\leftarrow n} \\
&= \left[\int_{\mathbf{k}} \sum_{\substack{n\in\text{occ}\\m\in\text{unocc}}} (-eR^c_{mn})f^{\text{FD}}_{nm}\frac{2\pi}{\hbar}\left|\sum_a\langle m|\frac{ie}{\hbar\omega}E_a(\omega)\partial_a H|n\rangle\right|^2\delta(\hbar\omega_{mn}-\hbar\omega)\right] + (\omega\to-\omega) \\
&= -\frac{2\pi e^3}{\hbar}\int_{\mathbf{k}} \sum_{n,m,a,b} f^{\text{FD}}_{nm}R^c_{mn}\frac{\langle n|\partial_b H|m\rangle}{\hbar\omega_{mn}}\frac{\langle m|\partial_a H|n\rangle}{\hbar\omega_{mn}}E_a(\omega)E_b(-\omega)\delta(\hbar\omega_{mn}-\hbar\omega) \\
&= -\frac{2\pi e^3}{\hbar^2}\int_{\mathbf{k}} \sum_{n,m,a,b} f^{\text{FD}}_{nm}R^c_{mn}r^b_{nm}r^a_{mn}\delta(\omega_{mn}-\omega)E_a(\omega)E_b(-\omega), \\
\partial_t j^c_{\text{inj}} &= \int_{\mathbf{k}} \sum_{n,m,a,b} (-e\Delta^c_{mn})f^{\text{FD}}_{nm}\mathcal{M}_{m\leftarrow n}(\omega) \\
&= -\frac{2\pi e^3}{\hbar^2}\int_{\mathbf{k}} \sum_{n,m} f^{\text{FD}}_{nm}\Delta^c_{mn}r^b_{nm}r^a_{mn}\delta(\omega_{mn}-\omega)E_a(\omega)E_b(-\omega),
\end{aligned} \tag{B1}
$$

where $\mathcal{M}_{m \leftarrow n}$ is the probability of the transition from n to m. We note that this Fermi golden rule calculation gives an overall (-1) sign that is absent in the results in Refs. [19,22], while they also take $-e$ as the electron charge. Also, our expressions differ from the results in Refs. [19,22] by the sign of ω in the electric fields.

APPENDIX C: TIME-REVERSAL TRANSFORMATION OF THE SECOND-ORDER OPTICAL CONDUCTIVITY

Let us consider the most general second-order optical conductivity tensor defined by

$$j^c(\tilde{\omega}) = \sigma^{c;ab}(\tilde{\omega}; \tilde{\omega}_1, \tilde{\omega}_2) E_a(\tilde{\omega}_1) E_b(\tilde{\omega}_2), \qquad \text{(C1)}$$

where $\tilde{\omega} = \tilde{\omega}_1 + \tilde{\omega}_2$ and $\tilde{\omega}_{1,2} = \omega_{1,2} + i\Gamma$. We can symmetrize the conductivity without loss of generality such that

$$\sigma^{c;ab}(\tilde{\omega}; \tilde{\omega}_1, \tilde{\omega}_2) = \sigma^{c;ba}(\tilde{\omega}; \tilde{\omega}_2, \tilde{\omega}_1). \qquad \text{(C2)}$$

The current and the electric field transform as

$$j^c(\tilde{\omega}) \rightarrow j'^c(\tilde{\omega}) = -j^c(-\tilde{\omega}),$$
$$E_a(\tilde{\omega}_1) \rightarrow E'_a(\tilde{\omega}_1) = E_a(-\tilde{\omega}_1), \qquad \text{(C3)}$$

under time reversal $t \rightarrow -t$. Equation (C1) is equivalent to $-j'^c(-\tilde{\omega}) = \sigma^{c;ab}(\tilde{\omega}; \tilde{\omega}_1, \tilde{\omega}_2) E'_a(-\tilde{\omega}_1) E'_b(-\tilde{\omega}_2)$. It can be written as

$$j'^c(\tilde{\omega}) = \sigma'^{c;ab}(\tilde{\omega}; \tilde{\omega}_1, \tilde{\omega}_2) E'_a(\tilde{\omega}_1) E'_b(\tilde{\omega}_2) \qquad \text{(C4)}$$

if we define $\sigma'^{c;ab}$ by

$$\sigma'^{c;ab}(\tilde{\omega}; \tilde{\omega}_1, \tilde{\omega}_2) = -\sigma^{c;ab}(-\tilde{\omega}; -\tilde{\omega}_1, -\tilde{\omega}_2)$$
$$= -\sigma^{c;ba}(-\tilde{\omega}; -\tilde{\omega}_2, -\tilde{\omega}_1). \qquad \text{(C5)}$$

In the case of the dc generation, where $\omega_1 = -\omega_2$, which reduces to

$$\sigma'^{c;ab}(\omega, \Gamma) = -\sigma^{c;ba}(\omega, -\Gamma), \qquad \text{(C6)}$$

where $\sigma^{c;ab}(\omega, \Gamma) = \sigma^{c;ab}(0; \omega + i\Gamma, -\omega + i\Gamma)$.

APPENDIX D: DERIVATION OF EQS. (9) AND (10)

Let $\mathcal{M}$ be a point-group symmetry operation: $x_a \rightarrow x'_a = \mathcal{M}_{ab} x_b$. The Bloch state transforms as

$$|\psi_{n\mathbf{k}}\rangle \rightarrow |\psi'_{n\mathbf{k}}\rangle = \hat{\mathcal{M}}|\psi_{n\mathcal{M}^{-1}\mathbf{k}}\rangle. \qquad \text{(D1)}$$

When the system has $\mathcal{M}$ symmetry (i.e., $\hat{\mathcal{M}}^{-1}H\hat{\mathcal{M}} = H$), $|\psi'_{n\mathbf{k}}\rangle = |\psi_{m\mathbf{k}}\rangle M_{mn}(\mathbf{k})$ is satisfied, where $M_{mn}(\mathbf{K})$ is a unitary matrix that is nonzero only when

$E_m(\mathbf{k}) = E_n(\mathcal{M}^{-1}\mathbf{k})$. Here, we *do not* assume that the system has $\mathcal{M}$ symmetry, and we focus on how quantities transform under $\mathcal{M}$. From the transformation property of the Bloch state, it follows that

$$|u_{n\mathbf{k}}\rangle \rightarrow |u'_{n\mathbf{k}}\rangle = \hat{\mathcal{M}}|u_{n\mathcal{M}^{-1}\mathbf{k}}\rangle. \qquad \text{(D2)}$$

Then,

$$r^a_{mn}(\mathbf{k}) \rightarrow r^{a'}_{mn}(\mathbf{k}) = g_{ab} r^b_{mn}(\mathcal{M}^{-1}\mathbf{k}). \qquad \text{(D3)}$$

We show this transformation property as follows:

$$\begin{aligned} r'^a_{mn}(\mathbf{k}) &\equiv \langle u'_{m\mathbf{k}}|i\partial_a|u'_{n\mathbf{k}}\rangle \\ &= \langle \hat{\mathcal{M}}u_{m\mathcal{M}^{-1}\mathbf{k}}|i\partial_a|\hat{\mathcal{M}}u'_{n\mathcal{M}^{-1}\mathbf{k}}\rangle \\ &= \frac{\partial(\mathcal{M}^{-1}k)_b}{\partial k_a} \langle \hat{\mathcal{M}}u_{m\mathcal{M}^{-1}\mathbf{k}}|i\partial_{(\mathcal{M}^{-1}k)_b}|\hat{\mathcal{M}}u'_{n\mathcal{M}^{-1}\mathbf{k}}\rangle \\ &= \mathcal{M}_{ab} r^b_{mn}(\mathcal{M}^{-1}\mathbf{k}), \end{aligned} \qquad \text{(D4)}$$

where we use that $(\mathcal{M}^{-1})_{ba} = \mathcal{M}_{ab}$. Similarly, we have

$$\begin{aligned} v'^a_{mn}(\mathbf{k}) & \\ &\equiv \hbar^{-1}\langle u'_{m\mathbf{k}}|\partial_a H'(\mathbf{k})|u'_{n\mathbf{k}}\rangle \\ &= \hbar^{-1}\langle \hat{\mathcal{M}}u_{m\mathcal{M}^{-1}\mathbf{k}}|\partial_a(\hat{\mathcal{M}}H(\mathcal{M}^{-1}\mathbf{k})\hat{\mathcal{M}}^{-1})|\hat{\mathcal{M}}u'_{n\mathcal{M}^{-1}\mathbf{k}}\rangle \\ &= \mathcal{M}_{ab} v^b_{mn}(\mathcal{M}^{-1}\mathbf{k}), \end{aligned} \qquad \text{(D5)}$$

where $H'(\mathbf{k}) = \hat{\mathcal{M}}H(\mathbf{k})\hat{\mathcal{M}}^{-1}$ and $H(\mathbf{k}) = e^{-i\mathbf{k}\cdot\hat{\mathbf{r}}}He^{i\mathbf{k}\cdot\hat{\mathbf{r}}}$ is the Bloch Hamiltonian. From these properties, one can find that

$$\sigma'^{c_1;a_1 b_1}_{dc}(\omega, \Gamma) = \mathcal{M}_{c_1 c}\mathcal{M}_{a_1 a}\mathcal{M}_{b_1 b}\sigma^{c;ab}_{dc}(\omega, \Gamma), \qquad \text{(D6)}$$

where $\sigma'^{c;ab}_{dc}$ is defined by the $\mathcal{M}$-transformed state $|u'_{n\mathbf{k}}\rangle$ and Hamiltonian $H'(\mathbf{k})$.

We can repeat this process for time reversal,

$$|u_{n\mathbf{k}}\rangle \rightarrow |\psi'_{n\mathbf{k}}\rangle = \hat{T}|u_{n,-\mathbf{k}}\rangle. \qquad \text{(D7)}$$

For the dipole matrix elements,

$$\begin{aligned} r'^a_{mn}(\mathbf{k}) &\equiv \langle u'_{m\mathbf{k}}|i\partial_a|u'_{n\mathbf{k}}\rangle \\ &= \langle \hat{T}u_{m,-\mathbf{k}}|i\partial_a|\hat{T}u'_{n,-\mathbf{k}}\rangle \\ &= \langle \hat{T}u_{m,-\mathbf{k}}|\hat{T}(-i)\partial_a u'_{n,-\mathbf{k}}\rangle \\ &= \langle (-i)\partial_a u'_{n,-\mathbf{k}}|u_{m,-\mathbf{k}}\rangle \\ &= \langle u'_{n,-\mathbf{k}}|i\partial_a|u_{m,-\mathbf{k}}\rangle \\ &= r^a_{nm}(-\mathbf{k}), \end{aligned} \qquad \text{(D8)}$$

where we use the antiunitary property of time reversal in the third line, and we integrate by parts in the fourth line:

$$\begin{aligned}
v'^a_{mn}(\mathbf{k}) &\equiv \hbar^{-1}\langle u'_{m\mathbf{k}}|\partial_a H'(\mathbf{k})|u'_{n\mathbf{k}}\rangle \\
&= \hbar^{-1}\langle \hat{T}u_{m,-\mathbf{k}}|\partial_a(\hat{T}H(-\mathbf{k})\hat{T}^{-1})|\hat{T}u'_{n,-\mathbf{k}}\rangle \\
&= \hbar^{-1}\langle \hat{T}u_{m,-\mathbf{k}}|\hat{T}\partial_a[H(-\mathbf{k})]u'_{n,-\mathbf{k}}\rangle \\
&= \hbar^{-1}\langle \partial_a[H(-\mathbf{k})]u'_{n,-\mathbf{k}}|u_{m,-\mathbf{k}}\rangle \\
&= -\hbar^{-1}\langle (\partial_a H)(-\mathbf{k})u'_{n,-\mathbf{k}}|u_{m,-\mathbf{k}}\rangle \\
&= -v^b_{nm}(-\mathbf{k}).
\end{aligned} \tag{D9}$$

We have

$$\sigma'^{c;ab}_{\mathrm{dc}}(\omega,\Gamma) = \sigma^{c;ab}_{\mathrm{dc}}(\omega,\Gamma), \tag{D10}$$

for linear shift and circular injection, and

$$\sigma'^{c;ab}_{\mathrm{dc}}(\omega,\Gamma) = -\sigma^{c;ab}_{\mathrm{dc}}(\omega,\Gamma), \tag{D11}$$

for circular shift and linear injection under time reversal, which proves Eqs. (9) and (10). Let us note that the time-reversal transformations derived here are consistent with Eq. (C6).

APPENDIX E: GENERAL FORM OF SHIFT CURRENT MATRIX ELEMENTS

In the clean limit, the dc conductivity corresponding to the shift current is

$$\sigma^{c;ab}_{\mathrm{shift}} = \frac{\pi e^3}{\hbar^2}\sum_{n,m}\int_{\mathbf{k}} f^{\mathrm{FD}}_{nm} I^{c;ab}_{nm}\delta(\omega_{mn}-\omega), \tag{E1}$$

where

$$I^{c;ab}_{nm} = -i(r^b_{nm}r^a_{mn,c} - r^b_{nm,c}r^a_{mn}) \tag{E2}$$

and

$$r^a_{mn,c} \equiv \partial_c r^a_{mn} - i(r^c_{mm} - r^c_{nn})r^a_{mn}. \tag{E3}$$

One can see that $I^{c;ab}_{nm}$ is identical to $(R^{c;a}_{mn} - R^{c;b}_{nm})r^b_{nm}r^a_{mn}$. Let us transform this to an expression involving only matrix elements of the derivatives of the Hamiltonian. Here, it is enough to consider $n \in$ occ and $m \in$ unocc because of the Fermi-Dirac distribution function. We first use Eq. (A2) to write the derivative of r^a_{mn} in terms of the velocity matrix elements:

$$\begin{aligned}
\partial_c r^a_{mn} &= \partial_c\left(\frac{v^a_{mn}}{i\omega_{mn}}\right) \\
&= \frac{1}{i\omega_{mn}}\left[\partial_c v^a_{mn} - v^a_{mn}\frac{\partial_c\omega_{mn}}{\omega_{mn}}\right].
\end{aligned} \tag{E4}$$

The derivative of the velocity matrix element can be decomposed further as

$$\begin{aligned}
\partial_c v^a_{mn} &= \hbar^{-1}\langle m|\partial_a\partial_c H|n\rangle + i\hbar^{-1}[r^c,\partial_a H]_{mn} \\
&= w^{ac}_{mn} + ir^c_{mm}v^a_{mn} - iv^a_{mm}r^c_{mn} \\
&\quad + ir^c_{mn}v^a_{nn} - iv^a_{mn}r^c_{nn} \\
&\quad + i\sum_{p\neq m,n}(r^c_{mp}v^a_{pn} - v^a_{mp}r^c_{pn}) \\
&= w^{ac}_{mn} + i(r^c_{mm} - r^c_{nn})v^a_{mn} - ir^c_{mn}\Delta^a_{mn} \\
&\quad + \sum_{p\neq m,n}\left(\frac{v^c_{mp}v^a_{pn}}{\omega_{mp}} - \frac{v^a_{mp}v^c_{pn}}{\omega_{pn}}\right),
\end{aligned} \tag{E5}$$

where we use Eq. (A1) and separate the $p = m$ or $p = n$ components from the $p \neq m$, n components in the summation in the second line, and we use Eq. (A1) again in the last line. Using the notation $\partial_c\omega_{nm} = v^c_{nn} - v^c_{mm} = \Delta^c_{nm}$, we have

$$\begin{aligned}
r^a_{mn,c} = \frac{1}{i\omega_{mn}}\Bigg[&w^{ac}_{mn} - \frac{v^c_{mn}\Delta^a_{mn} + v^a_{mn}\Delta^c_{mn}}{\omega_{mn}} \\
&+ \sum_{p\neq m,n}\left(\frac{v^c_{mp}v^a_{pn}}{\omega_{mp}} - \frac{v^a_{mp}v^c_{pn}}{\omega_{pn}}\right)\Bigg].
\end{aligned} \tag{E6}$$

Accordingly, we have

$$\begin{aligned}
r^b_{nm}r^a_{mn,c} = \frac{v^b_{nm}}{\omega^2_{mn}}\Bigg[&w^{ac}_{mn} - \frac{v^c_{mn}\Delta^a_{mn} + v^a_{mn}\Delta^c_{mn}}{\omega_{mn}}\Bigg] \\
&+ \frac{v^b_{nm}}{\omega^2_{mn}}\sum_{p\neq m,n}\left(\frac{v^c_{mp}v^a_{pn}}{\omega_{mp}} - \frac{v^a_{mp}v^c_{pn}}{\omega_{pn}}\right).
\end{aligned} \tag{E7}$$

Let us note that the last term in Eq. (E7) (the virtual transitions), in fact, should be summed over nondegenerate transitions; i.e., $\sum_{p\neq n,m}$ should be $\sum_{\omega_p\neq\omega_n,\omega_m}$. To see this, we note that the three-band term [which is the most clear from diagrammatic calculations with the substitution $\omega \to \omega + i\Gamma$ in the calculation of $\sigma^{c;ab}(\omega;\omega_1,\omega_2)$ [19,22]] is

$$\frac{v^b_{nm}}{\omega^2_{mn}}\sum_{p\neq m,n}\frac{v^c_{mp}v^a_{pn}}{\omega_{mp}+i\Gamma} - \frac{v^a_{mp}v^c_{pn}}{\omega_{pn}+i\Gamma}. \tag{E8}$$

Applying $r^a_{pn} = v^a_{pn}/i\omega_{pn}$ (and also $r^a_{mp} = v^a_{mp}/i\omega_{mp}$) gives Eq. (E7), assuming nondegeneracy of bands and taking $\Gamma \to 0$. However, in the degenerate case where $\omega_p = \omega_n$ for $p \neq n$, $v^a_{pn} = i\omega_{pn}r^a_{pn}$ does not imply $r^a_{pn} = v^a_{pn}/i\omega_{pn}$. Those degenerate cases should be omitted in the summation in Eq. (E7) because $v_{mp}v_{pn} \propto \omega_{pm}\omega_{np} = 0$ when degeneracy occurs.

APPENDIX F: SECOND-ORDER RESPONSE OF GENERAL k-LINEAR DIRAC HAMILTONIAN

Let us show that the following Hamiltonian has vanishing shift current and linear injection current responses:

$$H(\mathbf{k}) = \hbar \sum_{a,i=1}^{d} v_{ai} k_a \Gamma_i. \tag{F1}$$

Since this Hamiltonian is linear in momentum, the diamagnetic term w_{mn}^{ac} in Eq. (E7) vanishes. It follows that the integrand of the second-order optical conductivity is a tensor under the map $f(\mathbf{k})$, where $f^i = \hbar \sum_a v_{ai} k_a$, i.e.,

$$\sigma_{\mathrm{dc}}^{c;ab} = \int d^d k \partial_c f^k \partial_a f^i \partial_b f^j T_{ijk}, \tag{F2}$$

where T_{ijk} is a tensor in f space,

$$
\begin{aligned}
\sigma_{\mathrm{dc}}^{c;ab} &= \int d^d f \det\left(\frac{\partial f_i}{\partial k_a}\right)^{-1} \partial_c f^k \partial_a f^i \partial_b f^j T_{kij} \\
&= \hbar^3 v_{ai} v_{bj} v_{ck} \det(\hbar v_{ai}) \int d^d f T_{kij}(\mathbf{f}) \\
&= \hbar^6 v_{ai} v_{bj} v_{ck} \det(v_{ai}) \int d^d k T_{kij}(\mathbf{k}) \\
&= \hbar^6 v_{ai} v_{bj} v_{ck} \det(v_{ai}) \sigma_{\mathrm{dc},0}^{k;ij}, \tag{F3}
\end{aligned}
$$

where we changed the name of the variable from $\mathbf{f}$ to $\mathbf{k}$ in the third line, and $\sigma_0^{k;ij} = \int d^d k T_{kij}(\mathbf{k})$ is the conductivity for $\hbar v_{ai} = \delta_{ai}$. Since the shift current and linear injection current parts of $\sigma_{\mathrm{dc},0}^{k;ij}$ vanish, this finishes the proof.

APPENDIX G: QUANTUM GEOMETRIC TENSOR FOR DIRAC HAMILTONIANS

1. Quantum geometric tensor

The quantum geometric tensor of the occupied states is defined by

$$Q_{ab} = \sum_{n \in \mathrm{occ}} \sum_{m \in \mathrm{unocc}} r_{nm}^a r_{mn}^b, \tag{G1}$$

where $r_{nm}^a = i\langle n|\partial_a|m\rangle$. Its symmetric and antisymmetric parts, respectively, correspond to the quantum metric and the Berry curvature of the occupied states.

To see this, let us take occupied bands n_1 and n_2. Then,

$$
\begin{aligned}
\sum_{m \in \mathrm{unocc}} & r_{n_1 m}^a r_{mn_2}^b \\
&= \sum_{m \in \mathrm{unocc}} \langle n_1 | i\partial_a | m \rangle \langle m | i\partial_b | n_2 \rangle \\
&= \sum_{m \in \mathrm{unocc}} \langle \partial_a n_1 | m \rangle \langle m | \partial_b n_2 \rangle \\
&= \langle \partial_a n_1 | \partial_b n_2 \rangle - \sum_{p \in \mathrm{occ}} \langle \partial_a n_1 | p \rangle \langle p | \partial_b n_2 \rangle \\
&= \frac{1}{2}\left[\langle \partial_a n_1 | \partial_b n_2 \rangle - \sum_{p \in \mathrm{occ}} \langle \partial_a n_1 | p \rangle \langle p | \partial_b n_2 \rangle + (a \leftrightarrow b) \right] \\
&\quad + \frac{1}{2}\left[\langle \partial_a n_1 | \partial_b n_2 \rangle - \sum_{p \in \mathrm{occ}} \langle \partial_a n_1 | p \rangle \langle p | \partial_b n_2 \rangle - (a \leftrightarrow b) \right] \\
&= (g_{ab})_{n_1 n_2} - \frac{i}{2}(F_{ab})_{n_1 n_2}, \tag{G2}
\end{aligned}
$$

where the symmetric part

$$
\begin{aligned}
(g_{ab})_{n_1 n_2} &= \frac{1}{2}\left[\langle \partial_a n_1 | \partial_b n_2 \rangle - \sum_{p \in \mathrm{occ}} \langle \partial_a n_1 | p \rangle \langle p | \partial_b n_2 \rangle \right] \\
&\quad + (a \leftrightarrow b) \tag{G3}
\end{aligned}
$$

is the non-Abelian quantum metric of the occupied states, and the antisymmetric part

$$
\begin{aligned}
(F_{ab})_{n_1 n_2} &= i\langle \partial_a n_1 | \partial_b n_2 \rangle - i \sum_{p \in \mathrm{occ}} \langle \partial_a n_1 | p \rangle \langle p | \partial_b n_2 \rangle \\
&\quad - (a \leftrightarrow b) \\
&= \partial_a r_{n_1 n_2}^b - \partial_b r_{n_1 n_2}^a - i(r_{n_1 p}^a r_{pn_2}^b - r_{n_1 p}^b r_{pn_2}^a) \tag{G4}
\end{aligned}
$$

is the non-Abelian Berry curvature of the occupied states, where $r_{n_1 n_2}^a = i\langle n_1 | \partial_a | n_2 \rangle$ is the non-Abelian Berry connection of the occupied states. It follows that

$$
\begin{aligned}
Q_{ab} &= \sum_{n \in \mathrm{occ}} (g_{ab})_{nn} - \frac{i}{2}(F_{ab})_{nn} \\
&= g_{ab} - \frac{i}{2}F_{ab}. \tag{G5}
\end{aligned}
$$

2. Dirac Hamiltonian

Here, we consider the following $d_M \times d_M$ Dirac Hamiltonian:

$$H = f_0 + \sum_i f_i \Gamma_i. \tag{G6}$$

Let us note that this kind of Hamiltonian describes generic two-band systems when $d_M = 2$ and generic PT-symmetric four-band systems with $(PT)^2 = -1$ when $d_M = 4$. Let us suppose that half of the bands are occupied. Then, since $\hbar\omega_{\text{unocc}} - \hbar\omega_{\text{occ}} = 2\sqrt{\sum_i f_i^2} = 2f$, we have

$$Q_{ab} = \frac{\hbar^2}{4f^2} \sum_{n \in \text{occ}} \sum_{m \in \text{unocc}} v_{nm}^a v_{mn}^b. \quad (G7)$$

Also, the velocity matrix elements are given by

$$\hbar v_{m \neq n}^a = \langle m|\partial_a H|n\rangle = \sum_i \partial_a f_i \langle m|\Gamma_i|n\rangle. \quad (G8)$$

It follows that

$$Q_{ab} = \frac{1}{4f^2} \sum_{i,j} \partial_a f^i \partial_b f^j \sum_{n \in \text{occ}} \sum_{m \in \text{unocc}} \langle n|\Gamma_i|m\rangle\langle m|\Gamma_j|n\rangle. \quad (G9)$$

Let us evaluate the summation

$$\sum_{n \in \text{occ}} \sum_{m \in \text{unocc}} \langle n|\Gamma_i|m\rangle\langle m|\Gamma_j|n\rangle$$

$$= \sum_{n \in \text{occ}} \left[\langle n|\Gamma_i\Gamma_j|n\rangle - \sum_{m \in \text{occ}} \langle n|\Gamma_i|m\rangle\langle m|\Gamma_j|n\rangle \right]. \quad (G10)$$

The first term is

$$\sum_{n \in \text{occ}} \langle n|\Gamma_i\Gamma_j|n\rangle = \sum_{n \in \text{occ}} \frac{1}{2} \langle n|\{\Gamma_i,\Gamma_j\}|n\rangle + \frac{1}{2} \langle n|[\Gamma_i,\Gamma_j]|n\rangle$$

$$= \frac{d_M}{2}(\delta_{ij} + iJ_{ij}), \quad (G11)$$

where we use the property of Gamma matrices $\{\Gamma_i,\Gamma_j\} = 2\delta_{ij}$ and define

$$J_{ij} \equiv \frac{i}{d_M} \sum_{n \in \text{occ}} \langle n|[\Gamma_i,\Gamma_j]|n\rangle. \quad (G12)$$

As for the second term, we note that for $m, n \in \text{occ}$,

$$\langle m|\Gamma_j|n\rangle = -\frac{f_j}{f}\delta_{mn} = -\hat{f}_j\delta_{mn}. \quad (G13)$$

One can see this as follows. First, if we take the dot product of $\langle m|\Gamma_j|n\rangle$ and $\mathbf{f}$, we have $\langle m|\Gamma_j|n\rangle f_j = \langle m|f_j\Gamma_j|n\rangle = -f\delta_{mn}$. On the other hand, for a vector $\mathbf{n}$ perpendicular to $\mathbf{f}$, $\langle m|\Gamma_j|n\rangle n_j = \langle m|n_j\Gamma_j|n\rangle = 0$ because $n_j\Gamma_j$ anticommutes with $f_i\Gamma_i$. Since $\langle m|\Gamma_j|n\rangle$ is parallel to f_i, we have Eq. (G13). To sum up, we have

$$Q_{ab} = \sum_{i,j} \partial_a f^i \partial_b f^j \frac{d_M(\delta_{ij} - \hat{f}_i\hat{f}_j + iJ_{ij})}{8f^2}. \quad (G14)$$

In two-band systems, we have $J_{ij} = -\epsilon_{ijk}\hat{f}_k$ because $[\Gamma_i,\Gamma_j] = 2i\epsilon_{ijk}\Gamma_k$, where $\Gamma_i = \sigma_i$ is a Pauli matrix. On the other hand, in four-band systems described by a Dirac Hamiltonian, which are PT-symmetric four-band systems, we have $J_{ij} = 0$.

APPENDIX H: COMPATIBILITY BETWEEN METRIC, SYMPLECTIC FORM, AND CONNECTION

1. Metric connection

A connection γ_{ij}^k is called metric compatible if the inner product done by the metric is invariant under parallel transport [66]:

$$\nabla\eta = 0. \quad (H1)$$

In components, it reads

$$\partial_k\eta_{ij} - \eta_{il}\gamma_{kj}^l - \eta_{jl}\gamma_{ij}^l = 0, \quad (H2)$$

which can be written as

$$\begin{aligned} 0 &= (\nabla_k\eta)_{ij} \\ &= \mathbf{e}_i \cdot \nabla_k\eta \cdot \mathbf{e}_j \\ &= \nabla_k(\mathbf{e}_i \cdot \eta \cdot \mathbf{e}_j) - \nabla_k\mathbf{e}_i \cdot \eta \cdot \mathbf{e}_j - \mathbf{e}_i \cdot \eta \cdot \nabla_k\mathbf{e}_j \\ &= \partial_k\eta_{ij} - \gamma_{ki}^l\eta_{lj} - \eta_{il}\gamma_{kj}^l, \end{aligned} \quad (H3)$$

where we use the notation $\eta_{ij} = \mathbf{e}_i \cdot \eta \cdot \mathbf{e}_j$ and the definition $\nabla_k\mathbf{e}_i = \gamma_{ki}^l\mathbf{e}_l$. A metric compatible connection is called a metric connection. If a metric connection γ_{ij}^k satisfies the torsion-free condition $\gamma_{ij}^k = \gamma_{ji}^k$ (torsion is the antisymmetric part of γ_{ij}^k), it is uniquely determined to be

$$\gamma_{ij}^k = g^{kl}\frac{1}{2}(\partial_i\eta_{lj} + \partial_j\eta_{li} - \partial_l\eta_{ij}), \quad (H4)$$

and it is called the Levi-Civita connection.

2. Symplectic connection

Similarly, a connection is called a symplectic connection when it satisfies

$$\nabla\epsilon = 0. \quad (H5)$$

In components, it reads

$$\partial_k\epsilon_{ij} - \epsilon_{il}\gamma_{kj}^l + \epsilon_{jl}\gamma_{ki}^l = 0, \quad (H6)$$

which follows from

$$
\begin{aligned}
0 &= (\nabla_k \epsilon)_{ij} \\
&= \mathbf{e}_i \cdot \nabla_k \epsilon \cdot \mathbf{e}_j \\
&= \nabla_k (\mathbf{e}_i \cdot \epsilon \cdot \mathbf{e}_j) - \nabla_k \mathbf{e}_i \cdot \epsilon \cdot \mathbf{e}_j - \mathbf{e}_i \cdot \epsilon \cdot \nabla_k \mathbf{e}_j \\
&= \partial_k \epsilon_{ij} - \gamma_{ki}^l \epsilon_{lj} - \epsilon_{il} \gamma_{kj}^l \\
&= \partial_k \epsilon_{ij} + \gamma_{ki}^l \epsilon_{jl} - \epsilon_{il} \gamma_{kj}^l.
\end{aligned} \tag{H7}
$$

Unlike the metric compatibility, this condition alone cannot uniquely determine the connection, even after imposing the torsion-free condition $\gamma_{ij}^k = \gamma_{ji}^k$. However, adding metric compatibility makes the connection unique. On the generalized Bloch sphere, the Levi-Civita connection is the unique connection that is compatible with both the metric and the symplectic form.

APPENDIX I: GEOMETRIC INTERPRETATION OF THE CIRCULAR SHIFT CURRENT WITH MORE THAN TWO BANDS

Here, we show that the matrix element of the circular shift conductivity is related to the Christoffel symbol of the first kind defined between the n and m bands:

$$
\Gamma_{bca;nm} = \frac{1}{2} (\partial_c g_{ba;nm} + \partial_a g_{bc;nm} - \partial_b g_{ca;nm}), \tag{I1}
$$

where we define

$$
g_{ab;nm} = \mathrm{Re}(r_{nm}^a r_{mn}^b). \tag{I2}
$$

By using the identity

$$
\begin{aligned}
r_{nm}^b r_{mn,c}^a + r_{nm,c}^b r_{mn}^a &= r_{nm}^b \partial_c r_{mn}^a - i r_{nm}^b r_{mn}^a (r_{mm}^c - r_{nn}^c) \\
&\quad + (\partial_c r_{nm}^b) r_{mn}^a - i r_{nm}^b r_{mn}^a (r_{nn}^c - r_{mm}^c) \\
&= \partial_c (r_{nm}^b r_{mn}^a), \tag{I3}
\end{aligned}
$$

we obtain

$$
\begin{aligned}
\Gamma_{bca;nm} &= \frac{1}{2} (\partial_c g_{ba;nm} + \partial_a g_{bc;nm} - \partial_b g_{ca;nm}) \\
&= \frac{1}{2} \mathrm{Re}[\partial_c (r_{nm}^b r_{mn}^a) + \partial_a (r_{nm}^b r_{mn}^c) - \partial_b (r_{nm}^c r_{mn}^a)] \\
&= \frac{1}{2} \mathrm{Re}[r_{nm}^b r_{mn,c}^a + r_{nm,c}^b r_{mn}^a + r_{nm}^b r_{mn,a}^c + r_{nm,a}^b r_{mn}^c - r_{nm}^c r_{mn,b}^a - r_{nm,b}^c r_{mn}^a] \\
&= \frac{1}{2} \mathrm{Re}[2 r_{nm}^b r_{mn,c}^a + r_{nm}^b (r_{mn,a}^c - r_{mn,c}^a) - (r_{nm,b}^c - r_{nm,c}^b) r_{mn}^a - r_{nm}^c (r_{mn,b}^a - r_{mn,a}^b)], \tag{I4}
\end{aligned}
$$

where we add $0 = r_{nm}^b r_{mn,c}^a - r_{nm,c}^b r_{mn}^a - (r_{nm}^b r_{mn,c}^a - r_{nm,c}^b r_{mn}^a)$ in the last line and use $\mathrm{Re}(r_{nm,a}^b r_{mn}^c) = \mathrm{Re}(r_{nm}^c r_{mn,a}^b)$ for the last term. Let us note that $r_{mn,a}^c - r_{mn,c}^a$ terms in the parentheses are virtual transitions, as can be seen from Eq. (E6). Thus, we have

$$
\Gamma_{bca,nm} = \mathrm{Re}[r_{nm}^b r_{mn,c}^a] + \text{virtual transitions}. \tag{I5}
$$

Equivalently, we find that the matrix element of the circular shift current is given by

$$
\begin{aligned}
& \mathrm{Re}[r_{nm}^b r_{mn,c}^a - r_{nm,c}^b r_{mn}^a] \\
&= \Gamma_{bca;nm} - \Gamma_{acb;nm} + \text{virtual transitions}. \tag{I6}
\end{aligned}
$$

An analogous proof for the complex part will be more challenging because it requires the calculation of the inverse quantum metric because $\tilde{\Gamma}_{bca} = \frac{1}{2} F_{bd} (g^{-1})^{de} \Gamma_{eca}$.

APPENDIX J: SYMMETRY TRANSFORMATIONS OF GEOMETRIC QUANTITIES

Under the transformation

$$
(t, x_a) \to (t', x_a') = ((-1)^{s_T} t, \mathcal{M}_{ab} x_b), \tag{J1}
$$

the quantum geometric tensor and the quantum geometric connection transform as

$$
\begin{aligned}
Q_{ba}(\mathcal{M}\mathbf{k}) &= \mathcal{M}_{bb'} \mathcal{M}_{aa'} Q_{b'a'}^*(\mathcal{M}^{-1}\mathbf{k}), \\
C_{bca}(\mathbf{k}) &= (-1)^{s_T} \mathcal{M}_{bb'} \mathcal{M}_{cc'} \mathcal{M}_{aa'} C_{b'c'a'}^*(\mathcal{M}^{-1}\mathbf{k}). \tag{J2}
\end{aligned}
$$

Equivalently, we can write them as

$$
\begin{aligned}
g_{ba}(\mathbf{k}) &= \mathcal{M}_{bb'} \mathcal{M}_{aa'} g_{b'a'}(\mathcal{M}^{-1}\mathbf{k}), \\
F_{ba}(\mathbf{k}) &= (-1)^{s_T} \mathcal{M}_{bb'} \mathcal{M}_{aa'} F_{b'a'}(\mathcal{M}^{-1}\mathbf{k}), \\
\Gamma_{bca}(\mathbf{k}) &= (-1)^{s_T} \mathcal{M}_{bb'} \mathcal{M}_{cc'} \mathcal{M}_{aa'} \Gamma_{b'c'a'}(\mathcal{M}^{-1}\mathbf{k}), \\
\tilde{\Gamma}_{bca}(\mathbf{k}) &= \mathcal{M}_{bb'} \mathcal{M}_{cc'} \mathcal{M}_{aa'} \tilde{\Gamma}_{b'c'a'}(\mathcal{M}^{-1}\mathbf{k}). \tag{J3}
\end{aligned}
$$

APPENDIX K: DETAILS OF FIRST-PRINCIPLES CALCULATIONS

Manganese germanate MnGeO$_3$ forms a rhombohedral ilmenite structure with a P-symmetric space group $R\bar{3}$ [73] [see Fig. 9(a)]. The unit cell contains two formula units (f.u.). It becomes antiferromagnetic below 38 K with the same unit cell [73]. Although the AF structure [Fig. 9(a)] breaks both T and P symmetries, AF MnGeO$_3$ with magnetic space group $-3'$ has the combined PT symmetry [42]. PrGeAl crystallizes in the body-centered tetragonal structure [see Fig. 9(b)] with a broken P symmetry space group $I4_1md$ [75]. The unit cell also contains two f.u. It becomes ferromagnetic at 16 K [44], and the FM structure [Fig. 9(b)] has no T symmetry nor PT symmetry.

The electronic band structure and magnetic properties of MnGeO$_3$ and PrGeAl are calculated based on first-principles density functional theory with the generalized gradient approximation (GGA) [77]. The experimental structural parameters for MnGeO$_3$ [73] and PrGeAl [75] are used in the present calculations. To better describe the Coulomb correlation among Mn $3d$ electrons and also among Pr $4f$ electrons, we adopt the GGA $+$ U scheme [78]. Following the recent studies [42,43], we use the effective U value of 4.0 eV for both Mn $3d$ and Pr $4f$ electrons. The calculations are performed using the accurate projector-augmented wave (PAW) method [79], as implemented in the Vienna *ab initio* simulation package (VASP) [80,81]. The fully relativistic PAW potentials are adopted in order to include the spin-orbit coupling (SOC) effect. Large plane-wave cutoff energies of 450 eV and 500 eV are used for MnGeO$_3$ and PrGeAl, respectively. For the Brillouin zone integration, k-point meshes of $12 \times 12 \times 12$ and $16 \times 16 \times 16$ are used for MnGeO$_3$ and PrGeAl, respectively. All the calculations are performed with an energy convergence within 10^{-6} eV between the successive iterations.

Here, we consider MnGeO$_3$ and PrGeAl, respectively, in the AF and FM states with the magnetic moments being parallel to the c axis. The calculated relativistic band structures of MnGeO$_3$ and PrGeAl are displayed in Figs. 10(a) and 10(b), respectively. They are both semi-metals with low density of states at the Fermi level (E_F) of 0.315 states/eV/f.u. and 0.133 states/eV/f.u., respectively. The calculated Mn spin magnetic moment in MnGeO$_3$ is 4.29 μ_B and that of Pr in PrGeAl is 1.89 μ_B. The calculated band structures agree well with those reported previously [42,43].

Nonlinear optical photocurrents are calculated based on the linear response formalism with the independent particle approximation, as described above. Specifically, the dc shift and injection photocurrent conductivity tensors are calculated using Eq. (4) in Sec. II. Since a large number of k-points are needed to get accurate NLO responses [82,83], we use the efficient Wannier function interpolation method based on maximally localized Wannier functions (MLWFs) [84–86]. For MnGeO$_3$, 68 MLWFs per unit cell of Mn d, Ge p, and O p orbitals are constructed by fitting to the GGA+U+SOC band structure. In PrGeAl, 76 MLWFs per
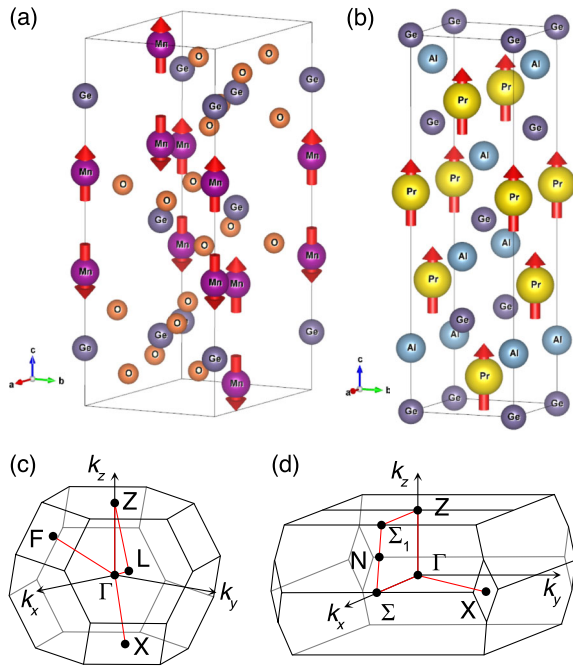

FIG. 9. Crystal and magnetic structures of (a) MnGeO$_3$ and (b) PrGeAl. The associated Brillouin zones are shown in panels (c) and (d), respectively.
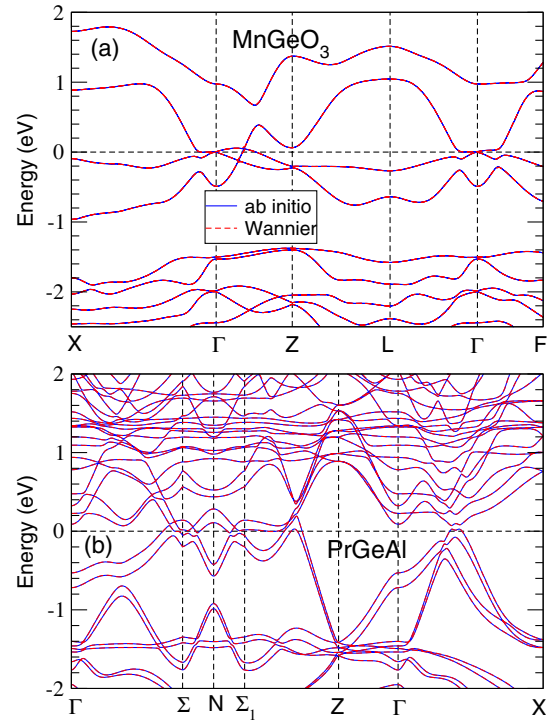

FIG. 10. Fully relativistic band structures of (a) antiferromagnetic MnGeO$_3$ and (b) ferromagnetic PrGeAl. The Fermi level (E_F) is at 0 eV.

unit cell of Pr d and f orbitals, as well as Ge p and Al sp orbitals, are adopted. The band structures obtained by the Wannier interpolation are nearly identical to those from the GGA+U+SOC calculations (see Fig. 10). The shift current conductivity tensors are then evaluated by taking very dense k-point meshes of $200 \times 200 \times 200$ for MnGeO$_3$ and of $160 \times 160 \times 220$ for PrGeAl. We find that the conductivity tensors obtained using such dense k-point meshes converge within a few percent. Here, we consider the "cold" semimetals; i.e., the Fermi-Dirac function in Eq. (4) is taken to be a step function. Furthermore, the Dirac δ function is replaced by a Lorentzian function with a broadening width of $\hbar\tau^{-1} = 10$ meV. Accordingly, in the injection conductivity calculations, we use the relaxation time τ given by $\hbar\tau^{-1} = 10$ meV.

[1] J. Liu, F. Xia, D. Xiao, J. G. de Abajo, and D. Sun, *Semimetals for High Performance Photodetection*, Nat. Mater. **19**, 830 (2020).

[2] W. Kraut and R. von Baltz, *Anomalous Bulk Photovoltaic Effect in Ferroelectrics: A Quadratic Response Theory*, Phys. Rev. B **19**, 1548 (1979).

[3] R. von Baltz and W. Kraut, *Theory of the Bulk Photovoltaic Effect in Pure Crystals*, Phys. Rev. B **23**, 5590 (1981).

[4] T. Morimoto and N. Nagaosa, *Topological Nature of Nonlinear Optical Effects in Solids*, Sci. Adv. **2**, e1501524 (2016).

[5] F. de Juan, A. G. Grushin, T. Morimoto, and J. E. Moore, *Quantized Circular Photogalvanic Effect in Weyl Semimetals*, Nat. Commun. **8**, 15995 (2017).

[6] N. Nagaosa and T. Morimoto, *Concept of Quantum Geometry in Optoelectronic Processes in Solids: Application to Solar Cells*, Adv. Mater. **29**, 1603345 (2017).

[7] J. E. Sipe and A. I. Shkrebtii, *Second-Order Optical Response in Semiconductors*, Phys. Rev. B **61**, 5337 (2000).

[8] T. Morimoto, S. Zhong, J. Orenstein, and J. E. Moore, *Semiclassical Theory of Nonlinear Magneto-Optical Responses with Applications to Topological Dirac/Weyl Semimetals*, Phys. Rev. B **94**, 245121 (2016).

[9] E. J. König, H.-Y. Xie, D. A. Pesin, and A. Levchenko, *Photogalvanic Effect in Weyl Semimetals*, Phys. Rev. B **96**, 075123 (2017).

[10] K. W. Kim, T. Morimoto, and N. Nagaosa, *Shift Charge and Spin Photocurrents in Dirac Surface States of Topological Insulator*, Phys. Rev. B **95**, 035134 (2017).

[11] Q. Ma, S.-Y. Xu, C.-K. Chan, C.-L. Zhang, G. Chang, Y. Lin, W. Xie, T. Palacios, H. Lin, S. Jia et al., *Direct Optical Detection of Weyl Fermion Chirality in a Topological Semimetal*, Nat. Phys. **13**, 842 (2017).

[12] L. Wu, S. Patankar, T. Morimoto, N. L. Nair, E. Thewalt, A. Little, J. G. Analytis, J. E. Moore, and J. Orenstein, *Giant Anisotropic Nonlinear Optical Response in Transition Metal Monopnictide Weyl Semimetals*, Nat. Phys. **13**, 350 (2017).

[13] X. Yang, K. Burch, and Y. Ran, *Divergent Bulk Photovoltaic Effect in Weyl Semimetals*, arXiv:1712.09363.

[14] L. E. Golub and E. L. Ivchenko, *Circular and Magneto-induced Photocurrents in Weyl Semimetals*, Phys. Rev. B **98**, 075305 (2018).

[15] F. Flicker, F. de Juan, B. Bradlyn, T. Morimoto, M. G. Vergniory, and A. G. Grushin, *Chiral Optical Response of Multifold Fermions*, Phys. Rev. B **98**, 155145 (2018).

[16] Y. Zhang, H. Ishizuka, J. van den Brink, C. Felser, B. Yan, and N. Nagaosa, *Photogalvanic Effect in Weyl Semimetals from First Principles*, Phys. Rev. B **97**, 241118(R) (2018).

[17] G. B. Osterhoudt, L. K. Diebel, M. J. Gray, X. Yang, J. Stanco, X. Huang, B. Shen, N. Ni, P. J. W. Moll, Y. Ran et al., *Colossal Mid-Infrared Bulk Photovoltaic Effect in a Type-I Weyl Semimetal*, Nat. Mater. **18**, 471 (2019).

[18] J. Ma, Q. Gu, Y. Liu, J. Lai, P. Yu, X. Zhuo, Z. Liu, J.-H. Chen, J. Feng, and D. Sun, *Nonlinear Photoresponse of Type-II Weyl Semimetals*, Nat. Mater. **18**, 476 (2019).

[19] D. E. Parker, T. Morimoto, J. Orenstein, and J. E. Moore, *Diagrammatic Approach to Nonlinear Optical Response with Application to Weyl Semimetals*, Phys. Rev. B **99**, 045121 (2019).

[20] S. M. Young and A. M. Rappe, *First Principles Calculation of the Shift Current Photovoltaic Effect in Ferroelectrics*, Phys. Rev. Lett. **109**, 116601 (2012).

[21] B. M. Fregoso, T. Morimoto, and J. E. Moore, *Quantitative Relationship between Polarization Differences and the Zone-Averaged Shift Photocurrent*, Phys. Rev. B **96**, 075421 (2017).

[22] T. Holder, D. Kaplan, and B. Yan, *Consequences of Time-Reversal-Symmetry Breaking in the Light-Matter Interaction: Berry Curvature, Quantum Metric, and Diabatic Motion*, Phys. Rev. Research **2**, 033100 (2020).

[23] Y. G. Semenov, X. Li, and K. W. Kim, *Tunable Photogalvanic Effect on Topological Insulator Surfaces via Proximity Interactions*, Phys. Rev. B **86**, 201401(R) (2012).

[24] N. Ogawa, R. Yoshimi, K. Yasuda, A. Tsukazaki, M. Kawasaki, and Y. Tokura, *Zero-Bias Photocurrent in Ferromagnetic Topological Insulator*, Nat. Commun. **7**, 12246 (2016).

[25] C.-K. Chan, N. H. Lindner, G. Refael, and P. A. Lee, *Photocurrents in Weyl Semimetals*, Phys. Rev. B **95**, 041104(R) (2017).

[26] Y. Zhang, T. Holder, H. Ishizuka, F. de Juan, N. Nagaosa, C. Felser, and B. Yan, *Switchable Magnetic Bulk Photovoltaic Effect in the Two-Dimensional Magnet* CrI$_3$, Nat. Commun. **10**, 3783 (2019).

[27] Z. Sun, Y. Yi, T. Song, G. Clark, B. Huang, Y. Shan, S. Wu, D. Huang, C. Gao, Z. Chen et al., *Giant Nonreciprocal Second-Harmonic Generation from Antiferromagnetic Bilayer* CrI$_3$, Nature (London) **572**, 497 (2019).

[28] P. Mendis, *Photocurrent in a Semiconductor without a Symmetry Center*, JETP Lett. **7**, 278 (1968).

[29] V. N. Genkin and P. M. Mednis, *Contribution to the Theory of Nonlinear Effects in Crystals with Account Taken of Partially Filled Bands*, JETP **27**, 609 (1968).

[30] B. I. Sturman and V. M. Fridkin, *The Photovoltaic and Photo-refractive Effects in Noncentrosymmetric Materials* (CRC Press, Philadelphia, 1992), Vol. 8.

[31] D. F. Liu, A. J. Liang, E. K. Liu, Q. N. Xu, Y. W. Li, C. Chen, D. Pei, W. J. Shi, S. K. Mo, P. Dudin et al., *Magnetic*

Weyl Semimetal Phase in a Kagomé Crystal, Science **365,** 1282 (2019).

[32] I. Belopolski, K. Manna, D. S. Sanchez, G. Chang, B. Ernst, J. Yin, S. S. Zhang, T. Cochran, N. Shumiya, H. Zheng *et al.*, *Discovery of Topological Weyl Fermion Lines and Drumhead Surface States in a Room Temperature Magnet*, Science **365,** 1278 (2019).

[33] N. Morali, R. Batabyal, P. K. Nag, E. Liu, Q. Xu, Y. Sun, B. Yan, C. Felser, N. Avraham, and H. Beidenkopf, *Fermi-Arc Diversity on Surface Terminations of the Magnetic Weyl Semimetal $Co_3Sn_2S_2$*, Science **365,** 1286 (2019).

[34] G. Xu, H. Weng, Z. Wang, X. Dai, and Z. Fang, *Chern Semimetal and the Quantized Anomalous Hall Effect in $HgCr_2Se_4$*, Phys. Rev. Lett. **107,** 186806 (2011).

[35] M. Hirschberger, S. Kushwaha, Z. Wang, Q. Gibson, S. Liang, C. A. Belvin, B. A. Bernevig, R. J. Cava, and N. P. Ong, *The Chiral Anomaly and Thermopower of Weyl Fermions in the Half-Heusler GdPtBi*, Nat. Mater. **15,** 1161 (2016).

[36] S. K. Kushwaha, Z. Wang, T. Kong, and R. J. Cava, *Magnetic and Electronic Properties of the Cu-Substituted Weyl Semimetal Candidate $ZrCo_2Sn$*, J. Phys. Condens. Matter **30,** 075701 (2018).

[37] J. Zou, Z. He, and G. Xu, *The Study of Magnetic Topological Semimetals by First Principles Calculations*, npj Comput. Mater. **5,** 96 (2019).

[38] H.-S. Jin, Y.-J. Song, W. E. Pickett, and K.-W. Lee, *Noncentrosymmetric Compensated Half-Metal Hosting Pure Spin Weyl Nodes, Triple Nodal Points, Nodal Loops, and Nexus Fermions*, Phys. Rev. Mater. **3,** 021201 (2019).

[39] P. Tang, Q. Zhou, G. Xu, and S.-C. Zhang, *Dirac Fermions in an Antiferromagnetic Semimetal*, Nat. Phys. **12,** 1100 (2016).

[40] N. P. Armitage, E. J. Mele, and A. Vishwanath, *Weyl and Dirac Semimetals in Three-Dimensional Solids*, Rev. Mod. Phys. **90,** 015001 (2018).

[41] Z. Lin, C. Wang, P. Wang, S. Yi, L. Li, Q. Zhang, Y. Wang, Z. Wang, Y. Sun, Z. Sun *et al.*, *Dirac Fermions in Antiferromagnetic FeSn Kagomé Lattices with Combined Space Inversion and Time Reversal Symmetry*, Phys. Rev. B **102,** 155103 (2020).

[42] Y. Xu, L. Elcoro, Z. Song, B. J. Wieder, M. G. Vergniory, N. Regnault, Y. Chen, C. Felser, and B. A. Bernevig, *High-Throughput Calculations of Antiferromagnetic Topological Materials from Magnetic Topological Quantum Chemistry*, arXiv:2003.00012.

[43] G. Chang, B. Singh, S.-Y. Xu, G. Bian, S.-M. Huang, C.-H. Hsu, I. Belopolski, N. Alidoust, D. S. Sanchez, H. Zheng *et al.*, *Magnetic and Noncentrosymmetric Weyl Fermion Semimetals in the R AlGe Family of Compounds (R = Rare Earth)*, Phys. Rev. B **97,** 041104(R) (2018).

[44] D. S. Sanchez, G. Chang, I. Belopolski, H. Lu, J.-X. Yin, N. Alidoust, X. Xu, T. A. Cochran, X. Zhang, Y. Bian *et al.*, *Observation of Weyl Fermions in a Magnetic Non-Centrosymmetric Crystal*, Nat. Commun. **11,** 3356 (2020).

[45] Recently, another process has been proposed for metallic systems, which was termed a resonant photovoltaic effect [46]. We do not consider this effect here.

[46] P. Bhalla, A. H. MacDonald, and D. Culcer, *Resonant Photovoltaic Effect in Doped Magnetic Semiconductors*, Phys. Rev. Lett. **124,** 087402 (2020).

[47] C. Aversa and J. E. Sipe, *Nonlinear Optical Susceptibilities of Semiconductors: Results with a Length-Gauge Analysis*, Phys. Rev. B **52,** 14636 (1995).

[48] F. de Juan, Y. Zhang, T. Morimoto, Y. Sun, J. E. Moore, and A. G. Grushin, *Difference Frequency Generation in Topological Semimetals*, Phys. Rev. Research **2,** 012017 (2020).

[49] We define $\sigma_{dc}^{\prime c;ab}$ by $j_{dc}^{\prime c} = \sigma_{dc}^{\prime c;ab} E_a' E_b'$, where $j^{\prime c_1} = \mathcal{M}_{c_1 c} j^c$ and $E_{a_1}' = \mathcal{M}_{a_1 a} E_{a_2}$.

[50] L. Onsager, *Reciprocal Relations in Irreversible Processes. I.*, Phys. Rev. **37,** 405 (1931).

[51] R. Kubo, *Statistical-Mechanical Theory of Irreversible Processes. I. General Theory and Simple Applications to Magnetic and Conduction Problems*, J. Phys. Soc. Jpn. **12,** 570 (1957).

[52] Y. Tokura and N. Nagaosa, *Nonreciprocal Responses from Non-centrosymmetric Quantum Materials*, Nat. Commun. **9,** 3740 (2018).

[53] S. V. Gallego, J. Etxebarria, L. Elcoro, E. S. Tasci, and J. M. Perez-Mato, *Automatic Calculation of Symmetry-Adapted Tensors in Magnetic and Non-magnetic Materials: A New Tool of the Bilbao Crystallographic Server*, Acta Crystallogr. Sect. A **75,** 438 (2019).

[54] B.-J. Yang and N. Nagaosa, *Classification of Stable Three-Dimensional Dirac Semimetals with Nontrivial Topology*, Nat. Commun. **5,** 4898 (2014).

[55] H. B. Nielsen and M. Ninomiya, *A No-Go Theorem for Regularizing Chiral Fermions*, Phys. Lett. **105B,** 219 (1981).

[56] E. Witten, *Three Lectures on Topological Phases of Matter*, Nuovo Cimento **39,** 313 (2016).

[57] If we allow the transformation of a 4×4 Dirac point to different kinds of nodes, other possibilities exist, which include the splitting of a Dirac point into two Weyl points or the inflating of a Dirac point to a nodal line. These require $m_{ab} \Gamma_a \Gamma_b$ terms. In the former case, each of the Weyl points can be understood in our framework. Understanding the second-order response of nodal lines appearing in the latter case is an interesting topic, but it is out of the scope of this work.

[58] A. A. Soluyanov, D. Gresch, Z. Wang, Q. Wu, M. Troyer, X. Dai, and B. A. Bernevig, *Type-II Weyl Semimetals*, Nature (London) **527,** 495 (2015).

[59] J. P. Provost and G. Vallee, *Riemannian Structure on Manifolds of Quantum States*, Commun. Math. Phys. **76,** 289 (1980).

[60] A. M. Cook, B. M. Fregoso, F. de Juan, S. Coh, and J. E. Moore, *Design Principles for Shift Current Photovoltaics*, Nat. Commun. **8,** 14176 (2017).

[61] In fact, the integrand should be $(C_{bca} - C_{acb}^*)/2$ since it has the form $(R_{mn}^{c,a} - R_{nm}^{c,b}) r_{nm}^b r_{mn}^a$, but C_{bca} gives the same value of the real part of the current. For linearly polarized light, the conductivity is symmetric under $a \leftrightarrow b$. In this case, $C_{bca} + C_{acb}^* + a \leftrightarrow b$ is real, such that it contributes to the imaginary part of the conductivity and thus to the imaginary part of the current. For circularly polarized light, since $C_{bca} + C_{acb}^* - a \leftrightarrow b$ is imaginary, the conductivity takes a real value, so it contributes to the imaginary part of the current for circularly polarized light.

[62] A metric having this property is called the Fubini-Study metric, so the quantum metric is often called the Fubini-Study metric [63].

[63] M. Kolodrubetz, D. Sels, P. Mehta, and A. Polkovnikov, *Geometry and Non-adiabatic Response in Quantum and Classical Systems*, Phys. Rep. **697,** 1 (2017).

[64] This property is shared by another connection, the non-Abelian Berry connection $A_{mn}^a = \langle m|i\partial_a|n\rangle$, but the difference is that γ_{ij}^k is the connection for the Bloch vector **f** while A_{mn}^a is the connection for the quantum state $|n\rangle$.

[65] I. Gelfand, V. Retakh, and M. Shubin, *Fedosov Manifolds*, arXiv:dg-ga/9707024.

[66] M. Nakahara, *Geometry, Topology and Physics* (IOP Publishing, Bristol, 2003).

[67] I. Sodemann and L. Fu, *Quantum Nonlinear Hall Effect Induced by Berry Curvature Dipole in Time-Reversal Invariant Materials*, Phys. Rev. Lett. **115,** 216806 (2015).

[68] Y. Gao and D. Xiao, *Nonreciprocal Directional Dichroism Induced by the Quantum Metric Dipole*, Phys. Rev. Lett. **122,** 227402 (2019).

[69] A. T. Rezakhani, D. F. Abasto, D. A. Lidar, and P. Zanardi, *Intrinsic Geometry of Quantum Adiabatic Evolution and Quantum Phase Transitions*, Phys. Rev. A **82,** 012321 (2010).

[70] Y.-Q. Ma, S. Chen, H. Fan, and W.-M. Liu, *Abelian and Non-Abelian Quantum Geometric Tensor*, Phys. Rev. B **81,** 245129 (2010).

[71] Z. Wang, Y. Sun, X.-Q. Chen, C. Franchini, G. Xu, H. Weng, X. Dai, and Z. Fang, *Dirac Semimetal and Topological Phase Transitions in A_3Bi (A = Na, K, Rb)*, Phys. Rev. B **85,** 195320 (2012).

[72] Z. Wang, H. Weng, Q. Wu, X. Dai, and Z. Fang, *Three-Dimensional Dirac Semimetal and Quantum Transport in Cd_3As_2*, Phys. Rev. B **88,** 125427 (2013).

[73] K. Tsuzuki, Y. Ishikawa, N. Watanabe, and S. Akimoto, *Neutron Diffraction and Paramagnetic Scattering from a High Pressure Phase of $MnGeO_3$ (Ilmenite)*, J. Phys. Soc. Jpn. **37,** 1242 (1974).

[74] F. Nastos and J. E. Sipe, *Optical Rectification and Current Injection in Unbiased Semiconductors*, Phys. Rev. B **82,** 235204 (2010).

[75] E. Gladyshevskii, N. Nakonechna, K. Cenzual, R. Gladyshevskii, and J.-L. Jorda, *Crystal Structures of $PrAl_xGe_{2-x}$ Compounds*, J. Alloys Compd. **296,** 265 (2000).

[76] H. Watanabe and Y. Yanase, *Chiral Photocurrent in Parity-Violating Magnet and Enhanced Response in Topological Antiferromagnet*, arXiv:2006.06908.

[77] J. P. Perdew, K. Burke, and M. Ernzerhof, *Generalized Gradient Approximation Made Simple*, Phys. Rev. Lett. **77,** 3865 (1996).

[78] S. L. Dudarev, G. A. Botton, S. Y. Savrasov, C. J. Humphreys, and A. P. Sutton, *Electron-Energy-Loss Spectra and the Structural Stability of Nickel Oxide: An LSDA + U Study*, Phys. Rev. B **57,** 1505 (1998).

[79] P. E. Blöchl, *Projector Augmented-Wave Method*, Phys. Rev. B **50,** 17953 (1994).

[80] G. Kresse and J. Hafner, *Ab Initio Molecular Dynamics for Liquid Metals*, Phys. Rev. B **47,** 558 (1993).

[81] G. Kresse and J. Furthmüller, *Efficient Iterative Schemes for Ab Initio Total-Energy Calculations Using a Plane-Wave Basis Set*, Phys. Rev. B **54,** 11169 (1996).

[82] G. Y. Guo, K. C. Chu, D. S. Wang, and C. G. Duan, *Linear and Nonlinear Optical Properties of Carbon Nanotubes from First-Principles Calculations*, Phys. Rev. B **69,** 205416 (2004).

[83] C.-Y. Wang and G.-Y. Guo, *Nonlinear Optical Properties of Transition-Metal Dichalcogenide MX_2 (M = Mo, W; X = S, Se) Monolayers and Trilayers from First-Principles Calculations*, J. Phys. Chem. C **119,** 13268 (2015).

[84] X. Wang, J. R. Yates, I. Souza, and D. Vanderbilt, *Ab Initio Calculation of the Anomalous Hall Conductivity by Wannier Interpolation*, Phys. Rev. B **74,** 195118 (2006).

[85] N. Marzari, A. A. Mostofi, J. R. Yates, I. Souza, and D. Vanderbilt, *Maximally Localized Wannier Functions: Theory and Applications*, Rev. Mod. Phys. **84,** 1419 (2012).

[86] J. Ibañez-Azpiroz, S. S. Tsirkin, and I. Souza, *Ab Initio Calculation of the Shift Photocurrent by Wannier Interpolation*, Phys. Rev. B **97,** 245143 (2018).